A Biophysical Model of Nonquantal Transmission at the Vestibular Hair Cell-Calyx Synapse: K_{LV} currents Modulate Fast Electrical and Slow K^+ potentials in the Synaptic Cleft

Aravind Chenrayan Govindaraju[1,2], Imran H. Quraishi[3], Anna Lysakowski[4], Ruth Anne Eatock[5], Robert M. Raphael[1,6]

[1]Department of Bioengineering, Rice University, Houston, TX

[2]Applied Physics Graduate Program, Rice University, Houston, TX

[3]Department of Neurology, Yale University School of Medicine, New Haven, CT

[4]Department of Anatomy and Cell Biology, University of Illinois at Chicago, IL

[5]Department of Neurobiology, University of Chicago, Chicago, IL

Author for correspondence:
Robert M Raphael
Dept of Bioengineering, MS 142
Rice University
Houston, TX
rraphael@rice.edu

The authors declare no competing interests.

Abstract

Vestibular hair cells transmit information about head position and motion across synapses to primary afferent neurons. At some of these synapses, the afferent neuron envelopes the hair cell, forming an enlarged synaptic terminal referred to as a calyx. The vestibular hair cell-calyx synapse supports nonquantal transmission (NQT), a neurotransmitter-independent mechanism that is exceptionally fast. The underlying biophysical mechanisms that give rise to NQT are not fully understood. Here we present a computational model of NQT that integrates morphological and electrophysiological data. The model predicts that NQT involves two processes: changes in cleft K^+ concentration, as previously recognized, and very fast changes in cleft electrical potential. A significant finding is that changes in cleft electrical potential are faster than changes in $[K^+]$ or quantal transmission. The electrical potential mechanism thus provides a basis for the exceptional speed of neurotransmission between type I hair cells and primary neurons and explains experimental observations of fast postsynaptic currents. The $[K^+]$ mechanism increases the gain of NQT. Both processes are mediated by current flow through low-voltage-activated K^+ (K_{LV}) channels located in both pre-synaptic (hair cell) and post-synaptic (calyx inner face) membranes. The model further demonstrates that the calyx morphology is necessary for NQT; as calyx height is increased, NQT increases in size, speed and efficacy at depolarizing the afferent neuron. We propose that the calyx evolved to enhance NQT and speed up signals that drive vestibular reflexes essential for stabilizing the eyes and neck and maintaining balance during rapid and complex head motions.

Significance Statement

The ability of the vestibular system to drive the fastest reflexes in the nervous system depends on rapid transmission of mechanosensory signals at vestibular hair-cell synapses. In mammals and other amniotes, afferent neurons form unusual large calyx terminals on certain hair cells, and transmission at those synapses includes nonquantal transmission (NQT), which avoids the synaptic delay of quantal transmission. We present a quantitative model that shows how NQT depends on the extent of the calyx covering the hair cell, and attributes the short latency of NQT to changes in synaptic cleft electrical potential caused by current flowing through open potassium channels in the hair cell. This previously undescribed mechanism may act at other synapses.

Introduction

The vestibular inner ear drives fast reflexes that stabilize the eyes and neck during rapid head motions (Huterer and Cullen 2002). The first synapses in the reflex pathway are from mechanosensory hair cells onto primary afferent nerve terminals. In mammals and other amniotes, many vestibular afferent terminals take the form of calyces around specialized type I hair cells. Transmission at these synapses has been inferred to be exceptionally fast (McCue and Guinan 1994), prompting speculation that it includes a direct, non-quantal component, different from the usual transmission mediated by exocytosis of glutamate from synaptic vesicles (quantal transmission). Intracellular recordings from calyx-bearing afferents provided evidence for non-quantal transmission (NQT) (Yamashita and Ohmori 1990) that persists in the presence of quantal transmission (Holt et al. 2007). NQT does not involve gap junctions, which are not found at these synapses (Gulley and Bagger-Sjöbäck 1979; Ginzberg 1984; Yamashita and Ohmori 1991). Here we present a model that succeeds in replicating key experimental observations of NQT at the vestibular type I – calyx synapse, provides biophysical mechanisms for two related components of NQT in the calyceal synaptic cleft: changes in K^+ concentration ($[K^+]_{SC}$) and changes in the cleft electrical potential (ϕ_{SC}), and shows how the two components combine to produce fast and slow components of NQT.

A key challenge for understanding transmission at the vestibular hair-cell calyx (VHCC) synapse is the lack of experimental access to the synaptic cleft and pre-and post-synaptic membranes. Early models (Chen 1995; Goldberg 1996) recognized that the elongated cleft space between the type I hair cell and enveloping calyx structure could provide increased electrical resistance and limit the diffusion of ions. In these formulations, hair cell transduction stimulates K^+ to flow from the hair cell into the cleft, depolarizing both hair cell and calyx primarily by K^+ accumulation, with negligible changes in the cleft electrical potential. Supporting this model are experimental results that emphasize the role of K^+ accumulation (Lim et al. 2011; Contini et al. 2012, 2017, 2020; Spaiardi et al. 2020). Alternative suggestions include accumulation in the cleft of glutamate released from synaptic vesicles (Dalet et al. 2012; Sadeghi et al. 2014) or protons (Highstein et al. 2014). Yet, there remains no clear biophysical explanation for how NQT occurs, whether it can follow fast vestibular stimuli and the extent to which it depends on calyx morphology.

To discern how NQT operates, we have developed a detailed model of the VHCC synapse based on the anatomy of the afferent calyx terminal and the biophysical properties of ion channels and transporters

expressed in the hair cell, calyx terminal and afferent fiber. Simulated responses of the VHCC model to hair bundle deflection and voltage-clamp steps agree with experimental data. Such validation gives us confidence in the model's predictions for sites with no experimental data, notably the narrow, inaccessible synaptic cleft. Results show that NQT at the VHCC synapse depends on the geometry of the calyx, involves modulation of both the electrical potential and K^+ concentration in the synaptic cleft, and is mediated primarily by currents through low-voltage-activated potassium (K_{LV}) conductances in the presynaptic and postsynaptic membranes ($g_{K,L}$ and K_V7, respectively). A major outcome of the model is that fast post-synaptic responses (Songer and Eatock 2013; Contini et al. 2020) arise from NQT-mediated changes in electrical potential in the synaptic cleft.

In other systems, changes in electrical potential in enclosed synaptic spaces have been shown to be important in processing stimuli with high time resolution (Vroman et al. 2013; Warren et al. 2016; Chiang et al. 2019). The importance of changes in cleft electrical potential has not been previously recognized at the VHCC synapse. By decoupling electrical potential from K^+ accumulation, we show that electrical potential changes in the cleft reduce the latency and extend the frequency response of nonquantal transmission. These predictions may explain the unexpectedly shorter delays at the hair-cell-afferent synapse that McCue and Guinan (1994) inferred for vestibular afferents with calyces relative to auditory afferents. Vestibular afferents are the first synapse in a neural circuit that encodes the fastest known reflexes in the nervous system: the vestibulo-ocular reflexes (VOR) (Huterer and Cullen 2002) and vestibulo-collic (neck) reflexes (VCR) (Colebatch and Rosengren 2019). Our model supports the proposal that the unique morphology of the calyx evolved to support fast synaptic transmission in response to increased locomotory challenges presented by the tetrapod transition from water to land (Eatock 2018; Curthoys et al. 2019).

General Description of the Model

The morphology of vestibular hair cells and calyces is highly conserved within particular zones of the vestibular epithelia (Lysakowski and Goldberg 1997, 2008). This model has been developed for an afferent calyx around a single type I hair cell ("simple calyx-only terminal") based on the geometry of a type I vestibular hair cell calyx from the striolar zone of the utricle and is thus representative of VHCC synapses in the striolar zone.

The model incorporates ion channels and transporters identified from experimental studies of type I hair cells and associated afferents to simulate the voltage response of the calyx to the mechanical stimulus: hair bundle deflection. Most of the parameters in the model are from published literature (cited in the **Supplementary Information (*SI*)**, **Tables S5, S6 and S7**); methods are provided for the unpublished data. The goal of the model is to understand the biophysical processes in the synaptic cleft that give rise to nonquantal transmission – defined as a change in the calyx potential in response to a change in hair cell potential that does not involve exocytosis of packets (vesicles or quanta) of neurotransmitter (in hair cells, glutamate). We do not explicitly consider quantal transmission, as the goal is to understand NQT as an independent phenomenon. In addition, mammalian calyces recorded in vitro often show only non-quantal transmission. The predictions of the model are compared to experimental results in which only NQT was present at the synapse. Simulations used physiological parameters from experimental data performed at room temperature.

The key parameters of interest are changes that occur in the electrical potential and K^+ concentration of the synaptic cleft, which is not experimentally accessible. The model incorporates capacitive and resistive currents across both the pre-synaptic hair cell and post-synaptic calyx membranes and uses continuity and electro-diffusion equations to describe the relationship between currents, electrical potentials and ion concentrations in the synaptic cleft. Using a finite element approach and COMSOL Multiphysics® software, we simulate the effects of changes in electrical potential in each model compartment and how these changes represent the mechanosensory signal as it travels from one compartment to the next. In the synaptic cleft spatiotemporal changes in both electrical potential and ion concentrations are simulated and result in spatially varying driving forces for currents along the hair cell and calyx inner face membranes. Initial and boundary conditions and full details on channel kinetics are provided in **SI**. The overall geometry, localization of ion channels and other relevant variables are presented in **Fig. 1**.

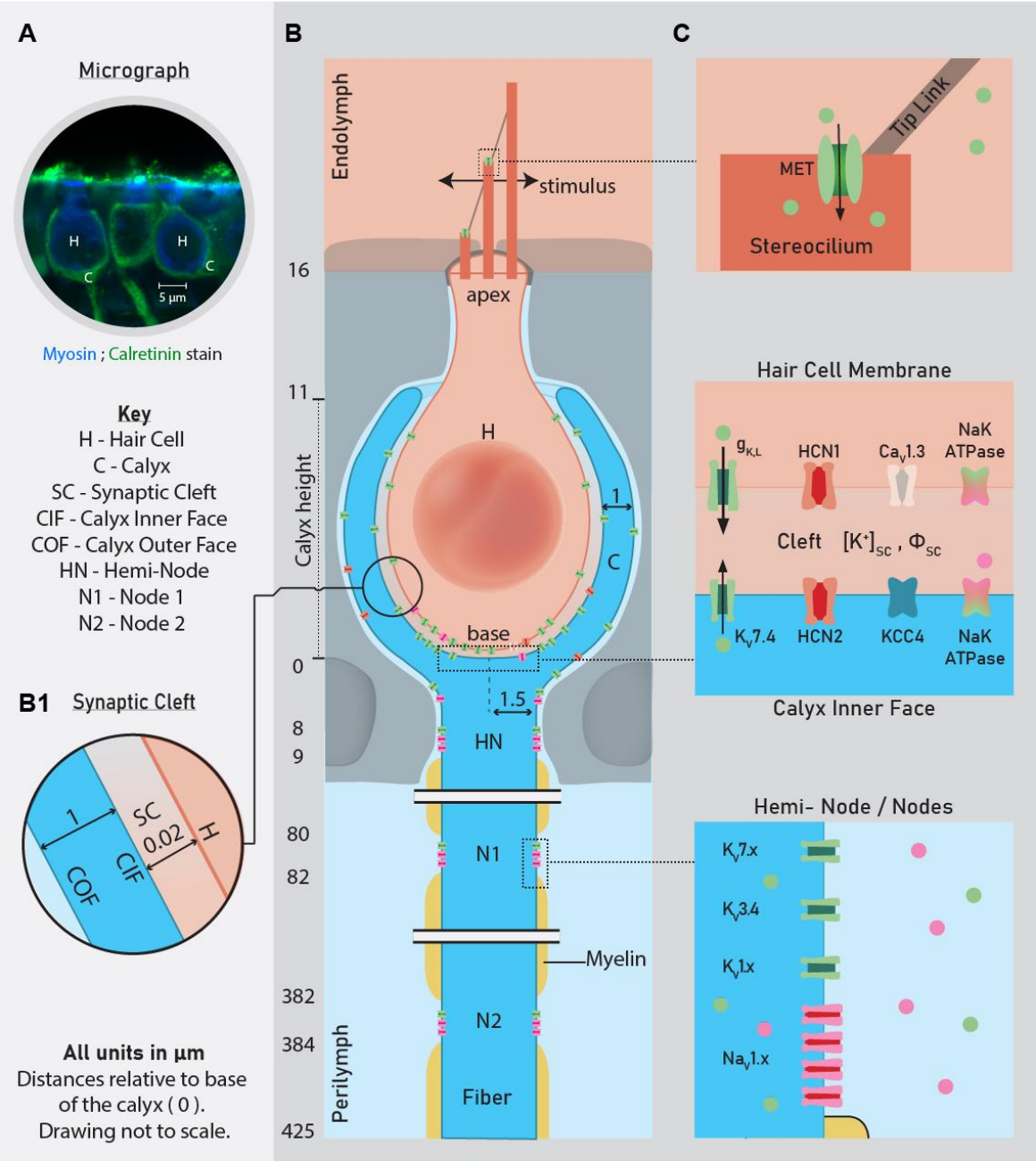

Fig. 1 – Graphic depiction of the VHCC model, illustrating key compartments, ion channels and transporters.

A, Confocal micrograph of type I hair cells (H, blue myosin immunolabel) within calyces (C, green calretinin immunolabel). Long-Evans adult rat utricle, striolar zone.

B, Geometry of a type I hair-cell-calyx synapse from central/striolar zones of rodent vestibular organs, and the dimensions used in the model. A 2D curve representing the hair cell, synaptic cleft and calyx was generated (**SI, Fig. S1**) based on measurements from Lysakowski et al. 2011, their Fig. 2C. Long-Evans adult rat crista, central zone. Dimensions were comparable (within 10%) to that of hair cells and calyces in **A.**

C, The ion channel types at different key locations in the model. See **SI, Tables S6 and S7** for sources of channel kinetics and distributions.

Results

Our goal is to use the VHCC model to delineate biophysical events that underlie NQT and to describe their effects on the mechanosensory signal carried by the calyx-bearing afferent, especially the response latency. We first describe the resting state of the VHCC compartments, then their responses to step bundle deflections. In each condition, we provide the model's output in terms of electrical potentials within the hair cell (ϕ_H), synaptic cleft (ϕ_{SC}), and calyx (ϕ_C) relative to an extracellular reference outside the VHCC; trans-membrane voltages for the membranes facing the synaptic cleft: hair cell membrane (V_H) and the calyx inner face membrane (V_{CIF}); K^+ and Na^+ concentrations in the synaptic cleft ($[K^+]_{SC}$, $[Na^+]_{SC}$); and key ion-channel currents across each membrane. The contributions to NQT of ϕ_{SC} and $[K^+]_{SC}$ are analyzed separately. We then compare model results to published data showing NQT in response to sinusoidal displacement of hair bundles and paired voltage clamp recordings from hair cells and calyces. Finally, to understand the extent to which NQT depends on calyx morphology, we analyze the effect of calyx height on the electrical and potassium potentials in the cleft and the response latency of the calyx.

Resting state of the system. The model was fully defined with no free parameters that required additional estimation. From the initial values and boundary conditions, we calculated the resting currents, ion concentrations, electrical potentials, and membrane voltages, using the stationary solver in COMSOL (***SI, Computational Methods***). At rest, the MET channels had a 10% open probability, yielding approximately –43 pA of current. The model produced hair cell and calyx resting potentials (ϕ_H: –78 mV, ϕ_C: –65 mV) that are consistent with reported resting ϕ_H and ϕ_C (Rennie and Correia 1994; Rennie et al. 1996; Rüsch and Eatock 1996; Chen and Eatock 2000; Sadeghi et al. 2014; Spaiardi et al. 2017). Model resting output values for which there are no experimental data for comparison are: ϕ_{SC} at the base of the synapse, +2 mV; $[K^+]_{SC}$ and $[Na^+]_{SC}$ at the base of the synapse, 7 mM and 129 mM, respectively. The non-zero value for ϕ_{SC} emerges from the properties of ion channels and transporters incorporated into the model.

These results were taken as the initial conditions from which to determine, with the time-dependent solver (COMSOL), changes in response to a stimulus. In all figures, the values at t = 0 show conditions at rest; often, however, we illustrate the model output for the step, which begins at 50 ms.

Synaptic response to a step displacement of the hair bundle. In **Fig. 2**, we illustrate the simulated response of sequential stages in the VHCC model to a positive (excitatory) step (+1 µm) of hair bundle displacement followed by a negative (inhibitory) displacement (–1 µm). The stimulus (**Fig. 2A**) is bundle

displacement viewed from above relative to resting position, taken mid-way up the bundle and parallel to the plane of the epithelium (**Fig. 1B**, 'stimulus'). Figure 2B illustrates the electrical potentials, membrane voltages and ion concentrations simulated in the model. The mechanotransduction current (I_{MET}) elicited by bundle stimulation is shown in **Fig. 2C**. Positive bundle displacement evoked a peak inward mechanotransduction current (I_{MET}) of ~400 pA, and the negative step reduced I_{MET} to 0. These changes in I_{MET} depolarized and hyperpolarized ϕ_H (**Fig. 2D**, modeled by **SI Eq. S2**), respectively, and altered hair cell basolateral (pre-synaptic) currents (**Fig. 3**). This model does not consider transducer adaptation, such that any decay (adaptation) of I_{MET} is driven by changes in ϕ_H, which changes the driving force on I_{MET}. Nonquantal transmission manifests as a change in calyx potential, ϕ_C, in response to changes in hair cell potential, ϕ_H. The small spikes (**Fig. 2D,E, arrows** and **Fig. 3A,C,E, vertical dashed line**) result from retrograde NQ transmission traveling back from the spiking calyx to the non-spiking hair cell, as discussed later.

Predicted Changes in Biophysical Properties of the Cleft ($\boldsymbol{\phi_{SC}}$, $[\boldsymbol{K}^+]_{SC}$, $[\boldsymbol{Na}^+]_{SC}$)

The model permits simulation of the biophysical properties of the cleft microenvironment which are not experimentally accessible. During NQT, the synaptic cleft potential, ϕ_{SC}, changes as shown in **Fig. 2D,D1.** The dynamic changes in ϕ_{SC} (modeled by **SI Eq. S5**) allow calculation of pre-synaptic (V_H) and post-synaptic (V_{CIF}) membrane voltages (**Fig. 2E**). V_H and V_{CIF} appear similar to the intracellular potentials with respect to ground (ϕ_H and ϕ_C, **Fig. 2D,E**), which can be physically measured, but there are important differences (compare **Fig. 2D1 and E1**). **Fig. 2F** shows the predicted changes in potassium concentration $[K^+]_{SC}$ and sodium concentration $[Na^+]_{SC}$ in the synaptic cleft at its base. For the simulated bundle stimulation, K^+ accumulation was accompanied by Na^+ depletion in the synaptic space, similar to a previous electrodiffusion model that considered the effect of the cleft on the hair cell receptor potential (Soto et al. 2002). In our VHCC model the changes in ion concentrations in the cleft are caused by altered ionic currents, mostly through channels in the pre-synaptic and post-synaptic membranes, and the axial electro-diffusion of ions from the source (ion channels in the depth of the cleft) to the sink (apical edges of the calyx) (**Fig. 1, and SI Eqs. S3,S4**).

Synaptic cleft potential, $\boldsymbol{\phi_{SC}}$, rises much faster than the synaptic cleft potassium level, $[\boldsymbol{K}^+]_{SC}$. To more clearly illustrate the variables responsible for the speed of NQT we show the dynamic changes in potentials relative to ground, ϕ_H and ϕ_C (**Fig. 2E1**), trans-membrane voltages, V_H and V_{CIF} (**Fig. 2F1**), and

synaptic cleft potential, ϕ_{SC} (**Fig. 2G)** during the first 5 ms after the step. We also plot the equilibrium potential of K^+, (E_K), which reflects changes in synaptic cleft potassium level, $[K^+]_{SC}$ (**Fig. 2G)**.

Insight into the driving forces that underlie NQT is provided by the difference in the time courses of the change in ϕ_{SC}, V_{CIF} and E_K (**Fig. 2E,G**). At the onset of the positive step, the synaptic cleft potential, ϕ_{SC}, rises to +6 mV in less than 1 ms but the rise in E_K is slower, consistent with the slow rise in $[K^+]_{SC}$ (**Fig. 2G**). E_K rises slower than the change in voltage across the calyx inner face V_{CIF} (**Fig. 2E1**). This provides an important insight into the mechanism of NQT: the immediate driving force for change in the post-synaptic (calyx) membrane current is first the change in V_{CIF}, and only later does the change in potassium potential make a significant contribution.

While the VHCC model results agree with experiments that show that changes in $[K^+]_{SC}$ affect both hair cell and calyx signals (Lim et al. 2011; Contini et al. 2012, 2017; Spaiardi et al. 2020) the model shows a pivotal role for the synaptic cleft potential, ϕ_{SC}. The independent contributions of ϕ_{SC} and $[K^+]_{SC}$ to NQT are analyzed later.

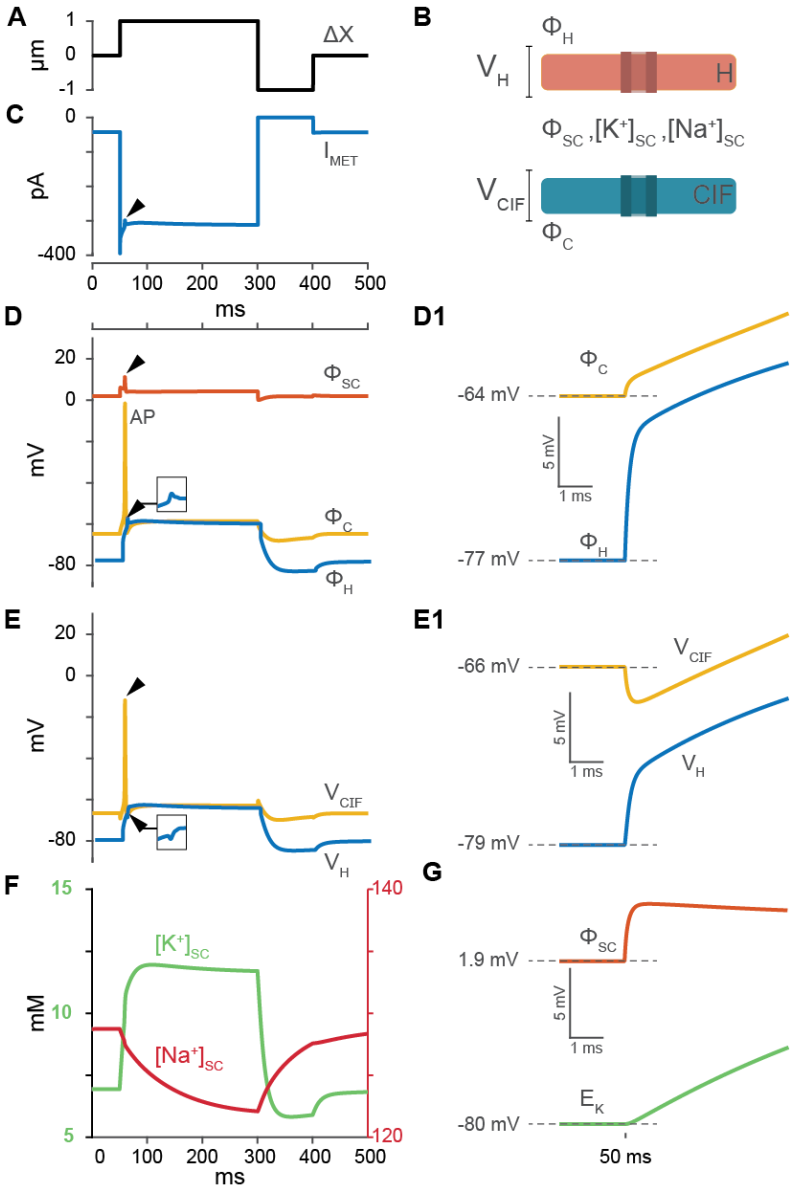

Fig. 2 – VHCC Model Predicts Fast (Electrical) and Slow (K+ Concentration) Forms of Anterograde Nonquantal Transmission in Response to Step Displacement of Hair Bundle, and Retrograde Transmission of the Calyceal Spike (AP).

A, +1 μm, 250-ms step followed by -1 μm 100 ms step displacement of the hair bundle.

B, Relation between the synaptic electrical potentials and membrane voltages.

C, Hair cell mechanotransduction current (I_{MET}).

D,D1, Electrical potentials in the hair cell (ϕ_H), synaptic cleft (ϕ_{SC}) and calyx (ϕ_C). **Arrowheads** show the retrograde transmission of the calyx AP stimulated by the anterograde transmission. Inset magnifies direction of inflection of ϕ_H.

D1, E1 and G, Expanded time axis between 48 ms and 55 ms. Step at 50 ms.

E,E1, Voltage across the basolateral hair cell membrane (V_H),the calyx inner face (V_{CIF}). Inset magnifies direction of inflection of V_H during the AP.

F, Potassium concentration $[K^+]_{SC}$ and sodium concentration $[Na^+]_{SC}$ in the synaptic cleft. Values shown are at the base of the synapse (or hair cell).

Contributions of Different Ion Channels to Nonquantal Transmission

The synaptic cleft is a dynamic system where electric potentials, ion concentrations and ionic currents interact. The changes in cleft potential and ion concentrations shown in **Fig. 2** are driven by currents through ion channels (see **SI, Table S6** for kinetics) on the hair cell basolateral membrane and on the calyx inner face and in turn modulate these currents (**Fig. 3**). Nonquantal transmission is bidirectional but below we first describe the roles of key channels during forward (hair cell to calyx, anterograde) nonquantal transmission.

Currents through open $g_{K,L}$ channels respond very rapidly to hair cell depolarization. The large low-voltage-activated K^+ conductance "$g_{K,L}$" is a distinctive feature of type I vestibular hair cells (Correia and Lang 1990; Rennie and Correia 1994; Rüsch and Eatock 1996). Because of its negative activation range, $g_{K,L}$ has a large open probability at the resting bundle position (here 54%), through which flows an outward K^+ current, $I_{K,L}$ (because hair cell membrane voltage is slightly positive (<1 mV) with respect to E_K across the hair cell membrane facing the cleft). At the onset of excitatory hair bundle stimulation, depolarization of the hair cell increases $I_{K,L}$ (**Fig. 3A**), altering both ϕ_{SC} and $[K^+]_{SC}$. $I_{K,L}$ is largely sustained, although there is a modest decrease reflecting the reduction in driving force as $[K^+]_{SC}$ increases and E_K depolarizes (**Fig. 3C**). During the negative bundle step (**Fig. 3B**), $I_{K,L}$ rapidly decreases, though not to zero, and then rises slightly as $[K^+]_{SC}$ gradually falls (**Fig. 3F**) and E_K becomes more negative (**Fig. 3C**). In our model conditions, the net $I_{K,L}$ was never inward (negative). However, by using the model to examine membrane currents as functions of location in the cleft and time, we noticed that inward $I_{K,L}$ can occur locally at the base of the hair cell during a negative step if E_K becomes positive to V_H (**Fig. 3D**, see crossover of V_H and E_K in insets). These results support the idea that $g_{K,L}$ may under certain conditions support inward K^+ currents into the hair cell and aid in K^+ clearance (Spaiardi et al. 2020).

In **Fig. 3** it is clear that the current through g_{KL} is fast, large, and non-inactivating, so that it closely follows the stimulus. Since g_{KL} is high in the resting state, the receptor-potential induced change in $I_{K,L}$ is not delayed by ion channel activation kinetics and is near instantaneous. $I_{K,L}$ rapidly changes the cleft electrical potential (**Fig. 3E,F**), which in turn rapidly alter currents through different low-voltage-activated K_{LV} channels in the calyx inner-face membrane.

Excitatory stimuli decrease K_V7 current into the cleft from the calyx. K_V7 channels located on the calyx inner face are partially open (29%) at resting potential (V_{CIF} = –68 mV) and supply K^+ to the synaptic cleft, helping to set resting levels of $[K^+]_{SC}$ and ϕ_{SC}. During positive bundle displacement, changes in voltage and E_K across the calyx inner face membrane (**Fig. 3C**) reduce outward K_V7 currents into the synaptic cleft except during the AP (**Fig. 3A**, see inset). During the negative bundle step, $I_{K,L}$ decreases, reducing $[K^+]_{SC}$ and ϕ_{SC} and, as a result, increasing the outward K_V7 current across the inner face membrane into the cleft (**Fig. 3D**, Right). Analysis of the magnitude and time course of the currents shows that $g_{K,L}$ in the hair cell and K_V7 channels in the calyx inner face membrane are primarily responsible for modulating $[K^+]_{SC}$, as suggested previously (Spaiardi et al. 2020).

Synaptic HCN channels establish resting conditions but have minimal effect on $[K^+]_{SC}$ and ϕ_{SC} during NQT. Hyperpolarization-activated cyclic-nucleotide-gated (HCN) channels are found on both sides of the VHCC synapse. Type I hair cells primarily express HCN1 channel subunits (Horwitz et al. 2011) and vestibular afferent neurons primarily express HCN2 subunits (Horwitz et al. 2014). Model results show that under physiological concentrations and potentials, HCN channels support a net inward current in both cells, mediated by influx of Na^+ ions, that is 10-100-fold smaller than outward K^+ currents through $g_{K,L}$ and K_V7 channels (**Fig. 3A**). In the model, we localized HCN1 to the hair cell and HCN2 to the calyx and found that both HCN channels contributed very small currents to either positive or negative step responses (**Fig. 3A,B**). This is explained by HCN channels' smaller whole cell conductance values (Horwitz et al. 2011, 2014) and their properties: the hyperpolarized activation voltage range, slow time constants, and mixed cationic currents (K^+ and Na^+) moving in opposite directions. Blocking HCN channels in the calyx has been shown to block NQ transmission (Contini et al. 2017), but only when the calyx was held at –100 mV, an unphysiological condition at which K_V7 channels would be closed. In the model, HCN channels, along with the Na^+/K^+-ATPase, contribute to the regulation of sodium concentration in the synaptic cleft (**Fig. 2F**) and appear more suited to homeostasis than active transmission. Based on currently available data it appears that HCN channels primarily contribute to the management of $[K^+]$ and $[Na^+]$ in the cleft space for optimal transmission and finely tune the resting potential of the calyx.

Retrograde transmission from calyx to hair cell. The model naturally captures retrograde transmission, a distinguishing feature of the VHCC synapse (Contini et al. 2017), defined as a change in hair cell potential caused by a change in calyx potential. This is especially pronounced during NQT-induced postsynaptic action potentials which occur for sufficiently large hair bundle displacements. An action potential in the fiber causes the calyx inner-face membrane to depolarize (**Fig. 3C; dashed line is at the time of the peak**

V_{CIF}) and increases outward current across the calyx inner face (**Fig. 3A**). The current responsible for retrograde transmission is largely carried by $g_{K,L}$ channels on the hair cell and K_V7 channels on the calyx inner face membrane: outward K^+ currents into the synaptic cleft increase, primarily through K_V7 channels (**Fig. 3A**; compare K_V7 and HCN2); ϕ_{SC} rises (**Fig. 3E, dashed line**); V_H becomes more negative (**Fig. 2E - V_H arrow and inset, Fig. 3C - V_H, dashed line**); outward K^+ currents from the hair cell, primarily through $g_{K,L}$ channels, decrease (**Fig. 3A -** see $g_{K,L}$ and HCN1); and the hair cell potential depolarizes (**Fig. 2D - ϕ_H, arrow and inset**). This illustrates that our VHCC model captures the bidirectional nature of nonquantal transmission, which theoretically could be used to modulate the sensitivity of both the calyx and the hair cell (Holt et al. 2017).

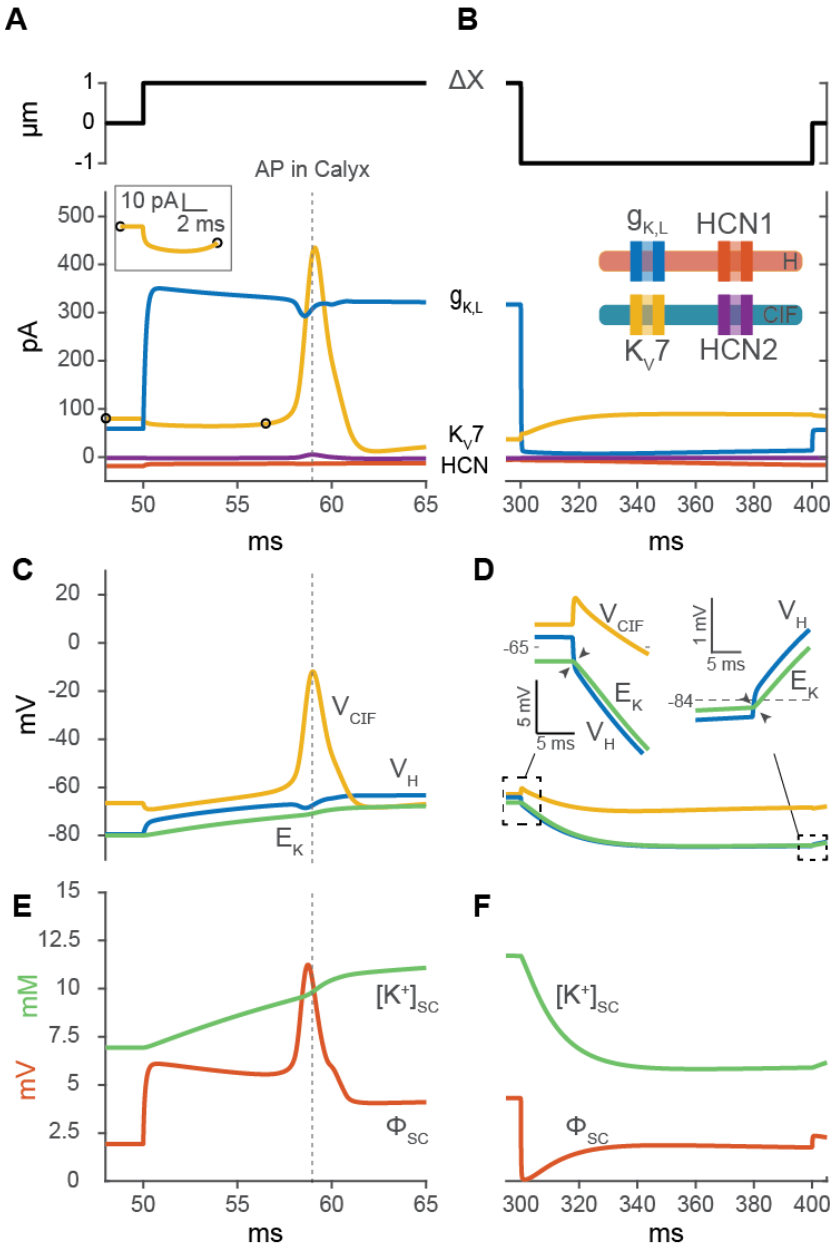

Fig. 3 – VHCC model predictions of key ionic currents during step bundle displacement and driving forces at the base of the synapse, and retrograde transmission of the action potential (AP). Net currents through $g_{K,L}$ (hair cells), K_V7 (calyx) and HCN channels (hair cell and calyx) in response to bundle displacement are shown at the onset of the excitatory step (**A**) and for the duration of the inhibitory step (**B**) of bundle displacement. Inset in A shows at higher gain the reduction in current through K_V7 at positive step onset.

C,D Driving forces, V_H, V_{CIF} and E_K at the base of the synapse during A and B respectively. Note the crossover of V_H and E_K during the negative displacement step shown in B.

E,F, ϕ_{SC} and $[K^+]_{SC}$ at the base of the synapse during A and B respectively.

In **A,C,E,** the dashed line marks time of AP peak in the calyx. Influence of the post-synaptic AP on driving forces and currents can be seen (retrograde transmission).

Role of the Synaptic Cleft in Nonquantal Transmission: $\boldsymbol{\phi_{SC}}$ and $[\boldsymbol{K}^+]_{\boldsymbol{SC}}$

The predictions of the VHCC model agree with experimental observations (Lim et al. 2011; Contini et al. 2012, 2017, 2020; Spaiardi et al. 2020) that support the hypothesis that K^+ currents through the basolateral membrane of the type I hair cell modulate $[K^+]_{SC}$ by changing E_K (Chen 1995; Goldberg 1996). The model further shows modulation of ϕ_{SC} that occurs on a faster time scale and alters both pre-synaptic and post-synaptic ionic currents. What are the relative contributions of $[K^+]_{SC}$ and ϕ_{SC} to NQT? Are both mechanisms necessary? What advantages do they provide? Are the contributions frequency-dependent? To answer these questions, we use the VHCC model to independently analyze ϕ_{SC} and $[K^+]_{SC}$ during both step and sinusoidal bundle displacements.

Isolation of the contributions of $\boldsymbol{\phi_{SC}}$ and $[\boldsymbol{K}^+]_{\boldsymbol{SC}}$ during step bundle displacements. We mathematically define two conditions: ϕ_{SC} modulation and $[K^+]_{SC}$ modulation. The ϕ_{SC} modulation-only condition is set by fixing $[K^+]_{SC}$ and $[Na^+]_{SC}$ at 5 mM and 140 mM, respectively, while ϕ_{SC} is allowed to vary as a function of ionic currents (**SI Eqs. S8-10**). The $[K^+]_{SC}$ modulation-only condition is set by fixing ϕ_{SC} at 0 mV and allowing $[K^+]_{SC}$ and $[Na^+]_{SC}$ to vary as functions of the ionic currents (**SI Eqs. S11-13**). **Figure 4** illustrates how ϕ_{SC} (blue), $[K^+]_{SC}$ (yellow), and both together (orange) shape NQ transmission at the onset of step bundle displacements of 0.3 and 1 μm (**Fig. 4A**). Changes in ϕ_C (**Fig. 4B**) are shown for all three conditions. To illustrate the increased speed of transmission we compared the time required for ϕ_C to rise by 1 mV in the $[K^+]_{SC}$-only condition and with both $[K^+]_{SC}$ and ϕ_{SC} enabled. As illustrated, changes in ϕ_{SC} increase the speed of NQT-mediated neurotransmission by 1.5 ms (1 μm step) and 1.8 ms (0.3 μm step).

The ϕ_{SC} mode contributes a nearly instantaneous change in calyx potential (ϕ_C) as seen at the onset of the step displacement. The fast rise at stimulus onset reflects the accompanying change in V_{CIF} which alters driving force for ions across the calyx inner face and is mediated by both capacitive membrane currents and resistive currents through open low-voltage-activated channels (further described in **Fig. 6**).

Figure 4C shows the considerably greater rate of change in calyx potential, $\frac{d\phi_C}{dt}$, for the ϕ_{SC}-only condition compared to the $[K^+]_{SC}$-only condition, and how both combine. The quick decay in $\frac{d\phi_C}{dt}$ in the ϕ_{SC}-only condition is a result of capacitive currents declining and resistive currents reaching a new steady state.

Overall, **Fig. 4** demonstrates that $[K^+]_{SC}$ modulation is responsible for the slow component of the rise in calyx potential. When ϕ_{SC} and $[K^+]_{SC}$ are allowed to vary concomitantly (orange traces), both fast and

slow components are seen. Comparing the rise of ϕ_C in the $[K^+]_{SC}$-only and $Both$ conditions clearly shows that the changes in ϕ_{SC} confer a ~1-2 ms advance to the calyx response (**Fig. 4B**). Thus, the modulation of ϕ_{SC} enables faster signal transmission between hair cell and calyx. The modulation of $[K^+]_{SC}$, although slower, ultimately supports greater depolarization of the calyx. For these inputs to the VHCC model, both mechanisms together did not trigger spiking for smaller hair bundle deflections and both were necessary to elicit spiking for the larger deflection. In the presence of an action potential, the response of the model at each stage is influenced by currents at the hemi-nodes and nodes of the afferent fiber (**SI, Eqs. S6, S7 and Table S6**). ϕ_C (**Fig. 4B**) resembles NQ responses of a rat utricular calyx to step bundle displacements (Songer and Eatock 2013 – their Fig. 5A).

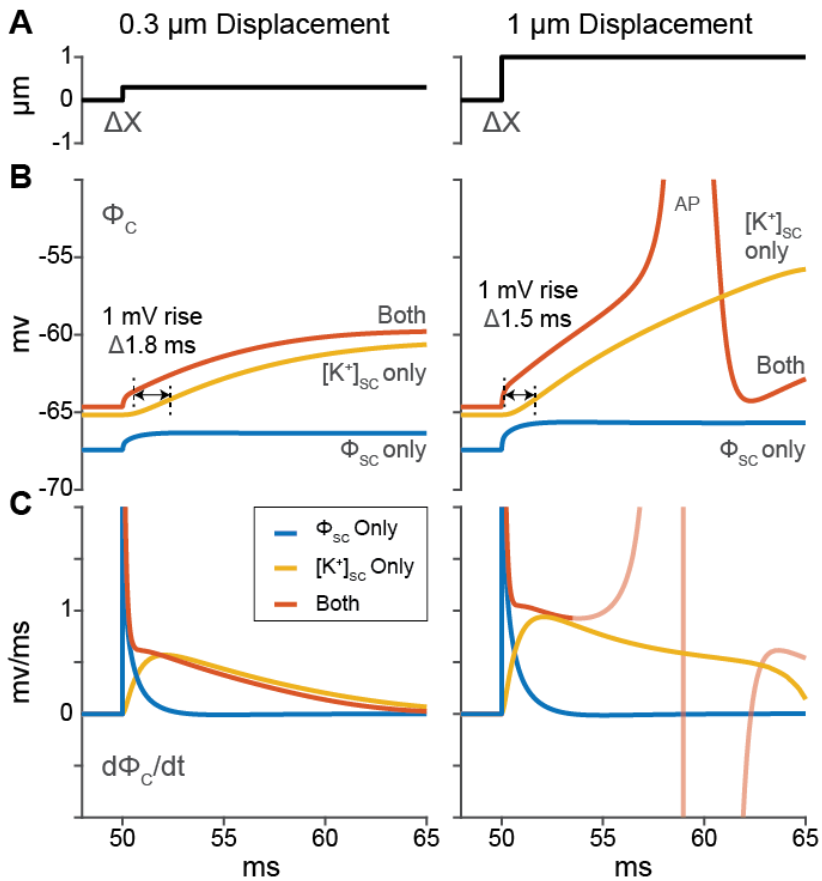

Fig. 4 – Contributions of ϕ_{SC} and $[K^+]_{SC}$ to nonquantal transmission at the onset of step bundle displacement. Simulation results with ϕ_{SC} modulation only (Blue), with $[K^+]_{SC}$ modulation only (Yellow) and with both enabled (Orange). **Left Column**: Simulation with 0.3 μm bundle displacement. **Right Column**: Simulation with 1 µm bundle displacement that evokes an action potential.
A, Bundle displacement stimulus.
B, Calyx Potential (ϕ_{SC}) rises faster when ϕ_{SC} is present, either alone or together with $[K^+]_{SC}$.
C, Rate of change of calyx potential. In both B and C, the first 15 ms after stimulus onset at 50 ms are shown. Note the difference between the ϕ_{SC} and $[K^+]_{SC}$ modulation-only components and the combined effects of both processes (Both). The larger stimulus (right) triggered an action potential, but only when in the 'Both' condition.

The electrical component of non-quantal transmission extends the frequency bandwidth toward higher frequencies

The effect of the electrical component of NQT on response latency to step stimuli manifests as an expansion of frequency bandwidth to include higher frequencies. Because most vestibular afferent data have been collected with sinusoidal head motion stimuli and presented as Bode plots of gain and phase of the fundamental component of the response, we tested the VHCC model with sinusoidal hair bundle input and used it to analyze the contributions of the ϕ_{SC} and $[K^+]_{SC}$ modulation-only components to the frequency response of the calyx.

The model captures NQ-driven firing in response to sinusoidal stimulus. We compared the model output with experimental NQ calyceal responses evoked by sinusoidal hair bundle stimulation delivered in 5-cycle bursts at frequencies between 2 and 100 Hz (Songer and Eatock, 2013; see their Fig. 5). Hair cell transduction and NQ transmission produced calyx potentials (**Fig. 5C**) that are consistent with whole-cell recordings from a calyx in the central striolar zone of the rat saccular epithelium (Songer and Eatock, 2013, their Fig. 5B,D) (**Fig. 5C**), including spikes for large stimuli (**Fig. 5B**). Both data and model show mid-band tuning, in that the calyx was most likely to spike for stimulus frequencies between 10 and 50 Hz. This relatively high-frequency tuning contributes to the sensitivity of striolar afferents to sound (McCue and Guinan 1994) and vibrations (Curthoys et al. 2019).

Frequency dependence of phase on $\boldsymbol{\phi_{SC}}$ and $[\boldsymbol{K}^+]_{\boldsymbol{SC}}$ modulation. The VHCC model enables us to separate the ϕ_{SC} and $[K^+]_{SC}$ components of NQ transmission evoked by a sinusoidal stimulation protocol (**Fig. 5A**). In **Fig. 5D,** we compare the phase and normalized gain of ϕ_H and ϕ_C responses in relation to the averaged peak values from five cycles of sinusoidal stimulus at 2 – 100 Hz for the ϕ_{SC} and $[K^+]_{SC}$ components. In the ϕ_C response, the ϕ_{SC} component exhibited broadband tuning while the $[K^+]_{SC}$ component exhibited low-pass behavior. A positive phase indicates that the maximal response of ϕ_H or ϕ_C is achieved before the maximal bundle displacement. For ϕ_H, at lower frequencies, the positive phase is primarily a function of $g_{K,L}$ activation (for kinetics, see **SI Table S6**): during the depolarizing half cycle, an appreciable increase in $g_{K,L}$ (>10% at 2 Hz) produces an increasing outward current that truncates the rise in ϕ_H before the peak of the bundle displacement. Likewise, for ϕ_C the positive phase at lower frequencies is primarily a function of the activation of low-voltage-activated K^+ channels within the calyx and fiber. The low-pass behavior of $[K^+]$ modulation can be explained by the time course of K^+ accumulation or depletion in the cleft (see **SI Eq. S3**). The influence of this effect is typically slow due to the greater number of ions

necessary to change ion concentrations in comparison to the electrical potential. In contrast, modulation of ϕ_{SC} instantaneously affects trans-membrane voltage across both pre- and post-synaptic membranes, producing capacitive currents and resistive (ionic) currents through open channels. This explains the short response latency at the onset of a step stimulus and the expansion of the frequency range to high frequencies. **Fig. 5E** shows that the model captures the actual (non-normalized) gain as a function of frequency. It also shows how the [K^+] modulation mechanism amplifies the calyx potential at all frequencies but especially below 20 Hz. This effect is consistent with the increasing size of the $[K^+]_{SC}$ component relative to the ϕ_{SC} component with time during a displacement step, shown in **Fig. 4B**.

Overall, the modulation of ϕ_{SC} and $[K^+]_{SC}$ control capacitive and resistive currents by altering driving forces (V_m and E_K) to facilitate the modulation of electrical potential in the afferent calyx (ϕ_C) in response to hair cell mechanotransduction. Both mechanisms are consistent with the view that the calyx serves to reduce transmission latency at the VHCC synapse. ϕ_{SC} modulation increases speed of transmission across all frequencies, manifesting as shorter latency to step displacements (**Fig. 4B**) and less phase lag to sinusoidal displacements (**Fig. 5D**) than in the [K^+] modulation-only condition. The major contribution of the [K^+] modulation mechanism is to increase the gain of non-quantal transmission (**Figs. 4B and 5E**). For larger bundle stimulations the combined processes enable NQT to depolarize the calyx sufficiently during excitatory bundle displacement to initiate action potentials (**Figs. 4B and 5C**).

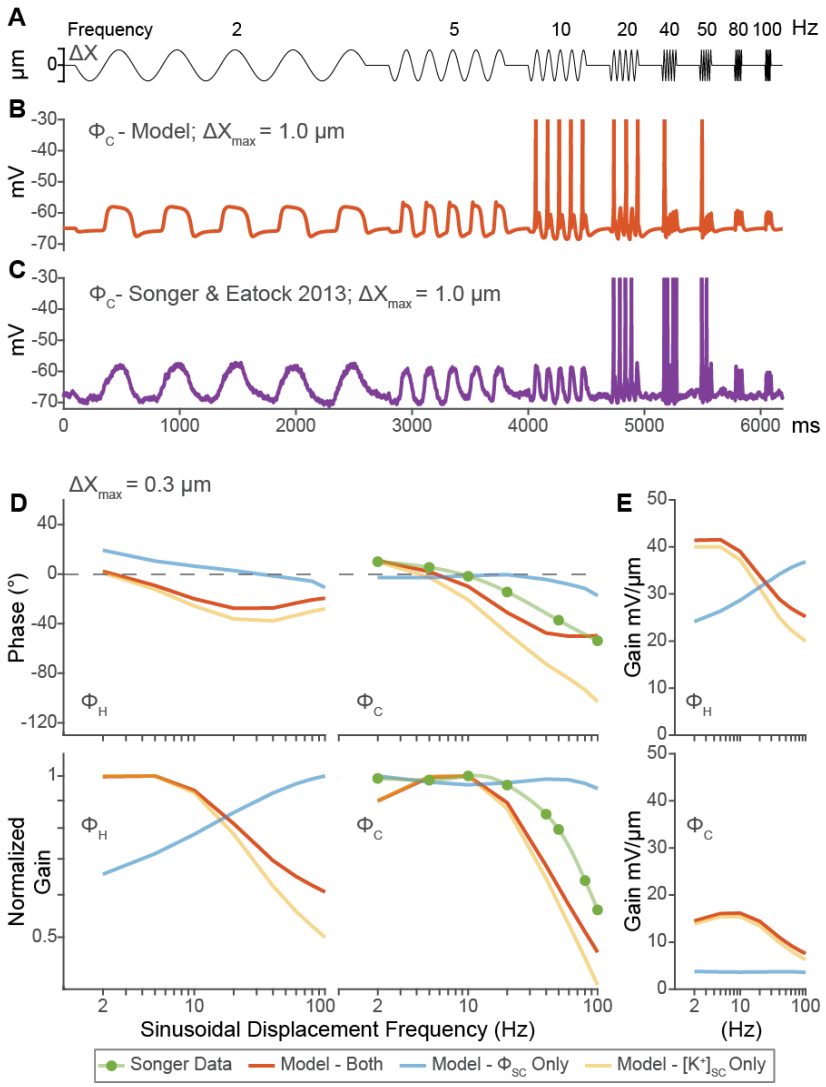

Fig. 5 - VHCC model reproduces key properties of the recorded waveform and tuning of a recorded NQT response to sinusoidal hair bundle stimuli. Here we simulate experiments from Songer & Eatock 2013 (their Figs. 5B and 5C).

A, Bundle displacement stimulus.

B, Modelled ϕ_C response to 1 µm bundle displacement.

C, Whole-cell current clamp recording from rat saccular calyx showing voltage response ϕ_C to ±1 µm sinusoidal bundle displacement (Songer and Eatock 2013, their Fig. 5B).

D, Bode plots showing frequency dependence of ϕ_C as phase (top) and normalized gain (bottom) for ±0.3 µm bundle displacement under different NQT conditions: ϕ_{SC} modulation-only (light blue), $[K^+]_{SC}$ modulation-only (light yellow) and *Both* (orange) conditions. In the ϕ_C response, the light green curve shows phase and gain characteristics for a different rat saccular calyx (Songer and Eatock 2013, their Fig. 5C).

E, Gain values corresponding to the normalized gains of ϕ_H and ϕ_C shown in D.

Paired voltage clamp recordings from hair cell and calyx provide evidence of changes in synaptic cleft potential

We have speculated that the speed of NQT depends on the large number of open $g_{K,L}$ channels in type I hair cells at resting potential. In this condition, the receptor potential instantaneously changes K^+ current flowing into the synaptic cleft, bypassing the time – on the order of 1- 100 ms - required to activate voltage-gated channels from the closed conformation. Experiments by Contini et al. (2020) on the turtle type I hair cell-calyx synapse address this hypothesis. We have used the VHCC model to simulate these experimental results and analyze them in terms of the ϕ_{SC} and $[K^+]_{SC}$ components.

Contini et al. (2020) did paired voltage-clamp recordings of whole-cell currents from type I hair cells and postsynaptic calyces. The hair cell was stepped to +20 mV from either -100 mV or -70 mV, while the calyx was held at either –100 mV or -70 mV. The step in hair cell potential evoked a fast net inward current across the calyx inner face membrane ($I_{ClF,R}$) (**Fig. 6 A1,A2** respectively). Contini et al. (2020) attribute this instance of fast NQ transmission to a covariation of currents through pre-synaptic and post-synaptic ion channels and term this "resistive coupling" (as opposed to capacitive coupling). However, the involvement of electrical potential in the synaptic cleft (ϕ_{SC}) was not considered. Here we show with the VHCC model that the difference in fast post-synaptic currents at the two different holding potentials reflects the different ion channel populations that are open in pre- and post-synaptic membranes and their effects on ϕ_{SC}.

The VHCC model was applied with either the $[K^+]_{SC}$-only condition or the $[K^+]_{SC}$ *and* ϕ_{SC} ("Both") condition, described earlier. We first examined the model's output for a calyx and hair cell holding potential of –100 mV (**Fig. 6, Left Column**), to compare with results from Contini et al. (2017, 2020). At this holding potential, $g_{K,L}$ and K_V7 channels were mostly closed and carried very little current. When ϕ_H was depolarized to +20 mV, significant capacitive currents across both the basolateral hair cell membrane ($I_{H,C}$) and the calyx inner face ($I_{ClF,C}$) preceded $g_{K,L}$ activation (**Fig. 6 D1,E1**) and contributed to the shape of the pulse in ϕ_{SC} at the start of the stimulus (**Fig. 6 B1**). This variation in synaptic cleft potential alters the driving force for currents through the calyx inner face and creates the "artifact" reported by Contini et al. 2020 (**Fig. 6 A1**), which we show to be a distinct resistive current (labeled as *). Both the time course and magnitude of change of the current simulated by the model matches closely with that seen by experiment. This current disappears when ϕ_{SC} is held at 0 in the '$[K^+]_{SC}$ -only' condition (faint

line, **Fig. 6 B1**). We suggest that the fast postsynaptic currents are not an artifact, but rather are evidence for changes in potential within the cleft in response to modulation of the hair cell potential.

The model predicts that when the calyx is held at –70 mV (**Fig. 6, Right Column**), an excitatory step in hair cell potential will evoke capacitive currents and outward current through open $g_{K,L}$ channels in the presynaptic membrane (**Fig. 6 D2,E2**) with equal speed (note the overlap in the rise of the currents), instantaneously elevating ϕ_{SC}. This hyperpolarizes the calyx inner face membrane (V_{CIF}) (**Fig. 6 B2**) and rapidly increases the inward driving force for K^+ across the calyx inner face, principally through K_V7 channels rather than HCN channels (**Fig. 6 E2**). This results in a distinctive and fast current (**) of similar time course to that seen by Contini et al. (2020) (compare **Fig. 6 A2 and B2**). The change in current size in the model exceeds that seen in the experiment, possibly reflecting differences in key channel properties (e.g., the voltage dependence and size of $g_{K,L}$) and calyx geometry between the model parameters (based on data from mice and rats) and the experimental data (from turtles). Note that the fast current (**) does not occur when ϕ_{SC} is held constant and only $[K^+]_{SC}$ allowed to vary (faded line, '$[K^+]_{SC}$ only', **Fig. 6 B2**).

The magnitude and unusual voltage dependence of $g_{K,L}$ serve NQT by driving rapid changes in ϕ_{SC}. Comparison of predicted responses to voltage steps from holding potentials of –100 mV and –70 mV demonstrate that large currents through open $g_{K,L}$ channels at -70 mV (but not -100 mV) produce a large, sustained change in ϕ_{SC} (compare **Fig. 6 E1,E2 and C1,C2**). The change in ϕ_{SC} simultaneously alters membrane voltage across the calyx inner face (V_{CIF}, compare **Fig. 6 C1 and C2**). In other words, open $g_{K,L}$ channels increase NQT. The unusual voltage dependence of $g_{K,L}$ ensures that many channels are open at rest, allowing fast ionic currents that drive fast change in ϕ_{SC}. $g_{K,L}$ also produces short membrane charging times that speed up membrane voltage changes. These results show the importance of both the large number and the unusually negative voltage dependence of $g_{K,L}$ channels.

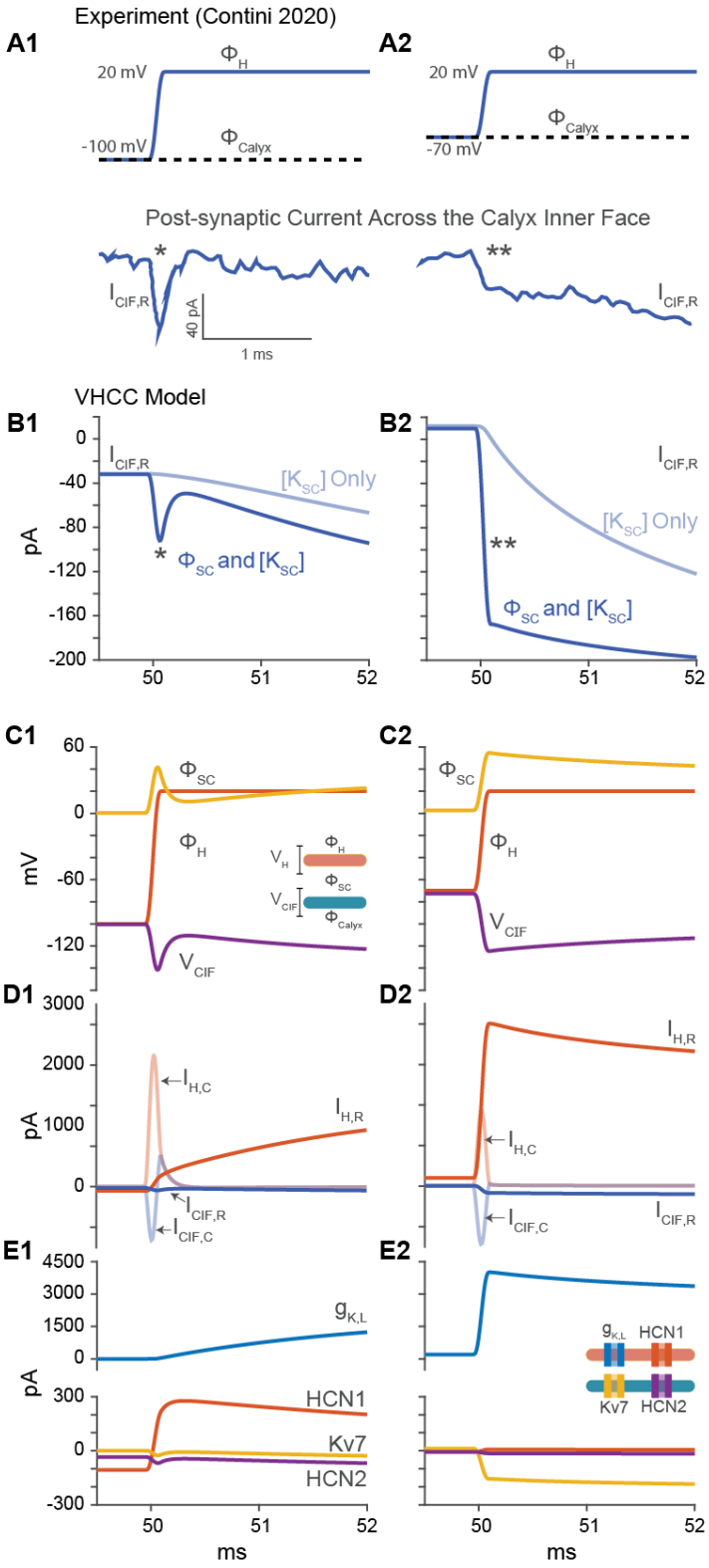

Fig. 6 - Changes in $g_{K,L}$ and calyceal K_{Lv} channels with voltage account for the marked effect of hair cell holding potential on NQT in paired voltage clamp recordings. Here we simulate the experiment of Contini et al. (2020, see their figure 10) on turtle type I-calyx synaptic transmission.

A, Voltage protocols and currents from experiment. Calyx Potential (ϕ_C) held at -100 mV. Hair cell potential stepped at 50 ms from holding potential of -100 mV to 20 mV (**A1**). Calyx Potential (ϕ_{Calyx}) held at -70 mV. Hair cell potential stepped at 50 ms from holding potential of -70 mV to 20 mV (**A2**). Currents reproduced from Contini et al. (2020).

B, Resistive post-synaptic current through the calyx inner face membrane, $I_{CIF,R}$. Note that fast currents (* and **) do not occur in the $[K]_{SC}$-only case (faded blue).

C, Electrical potential in the synaptic cleft and hair cell (ϕ_{SC}, ϕ_H) and voltage across hair cell basolateral (V_H) and calyx inner face (V_{CIF}) membranes. ϕ_{SC} is largely sustained when $g_{K,L}$ is already open, i.e., in the -70 mV condition - the small decay reflects the change in driving force as K^+ accumulates in the cleft.

D, Capacitive (C) and resistive (R) currents across the basolateral hair cell (I_{HC}) and calyx inner face (I_{CIF}) membranes. $I_{H,R}$ is sustained when $g_{K,L}$ is already open, i.e., in the -70 mV condition (**D2**).

E, Whole cell currents through individual ion conductances. From the non-physiological -100 mV holding potential (A1), HCN1 hair-cell current is prominent, fast and sustained, because HCN channels are open at -100 mV (**E1**). Note that from -70 mV holding potential (A2), $g_{K,L}$ current is fast and sustained and K_V7 current (gold) is the most prominent calyx current (**E2**).

Nonquantal Transmission Depends on Calyx Morphology

The simulations we have presented are for a calyx shape typical of many calyces in the central and striolar zones of rodent vestibular epithelia (**Fig. 1**). However, calyces vary in their shape in different regions of amniote vestibular epithelia (Lysakowski et al. 2011) and shorter "proto-calyces" are reported to exist in fish and amphibians (Honrubia et al. 1989; Lanford and Popper 1996; Lysakowski and Goldberg 2004; Boyle et al. 2018). To address the effects of calyx geometry on the two components of nonquantal transmission, we studied both the steady-state condition and the step response (**Fig. 7**) for different calyx heights, while retaining the same ion channel and transporter expression per unit area of membrane. As the calyx was truncated, both ϕ_{SC} and $[K^+]_{SC}$ were closer to perilymph values (0 mV and 5 mM respectively) at rest (**Fig. 7A,B Left**), had smaller responses to stimuli (**Fig. 7A,B Right**) and no spikes were initiated in the calyx stalk. However, the model does suggest that proto-calyces of anamniotes could accumulate K^+ that depolarizes the hair cell and calyx by ~2 mV (assuming a similar distribution of ion channels). On the other hand, elongation of the calyx height by 2 μm (relative to the standard geometry, **Fig. 1**) increased ϕ_{SC} and $[K^+]_{SC}$ at rest and the rate and magnitude of their stimulus-evoked changes, and reduced transmission latency. This greater height is found in the calyces of "dimorphic" afferents (Lysakowski et al. 2011), which have both calyx and bouton endings.

Fig. 7 shows that increasing calyx height increases the resting values of both ϕ_{SC} and $[K^+]_{SC}$, which depolarizes both the hair cell and calyx potentials, opening more ion channels at rest, increasing stimulus-evoked changes in both ϕ_{SC} and $[K^+]_{SC}$, increasing the likelihood of post-synaptic spiking and reducing first-spike latency with further increases in height (**Fig. 7A Right**; the occurrence of a calyx spike is evident in the ϕ_{SC} traces for the standard and extended calyx). Simulations of calyx heights at finer intervals indicated that NQT-initiated spiking required a calyx height within 95% of the value used in the VHCC model. These model results suggest that the central calyx height used in the model (11.3 μm) is at or near the minimal calyx height for NQT-driven spiking. Interestingly, once this minimal length is achieved, variations in calyx length have a significant effect on the magnitude and rate of NQT and time-to-spike in the calyx.

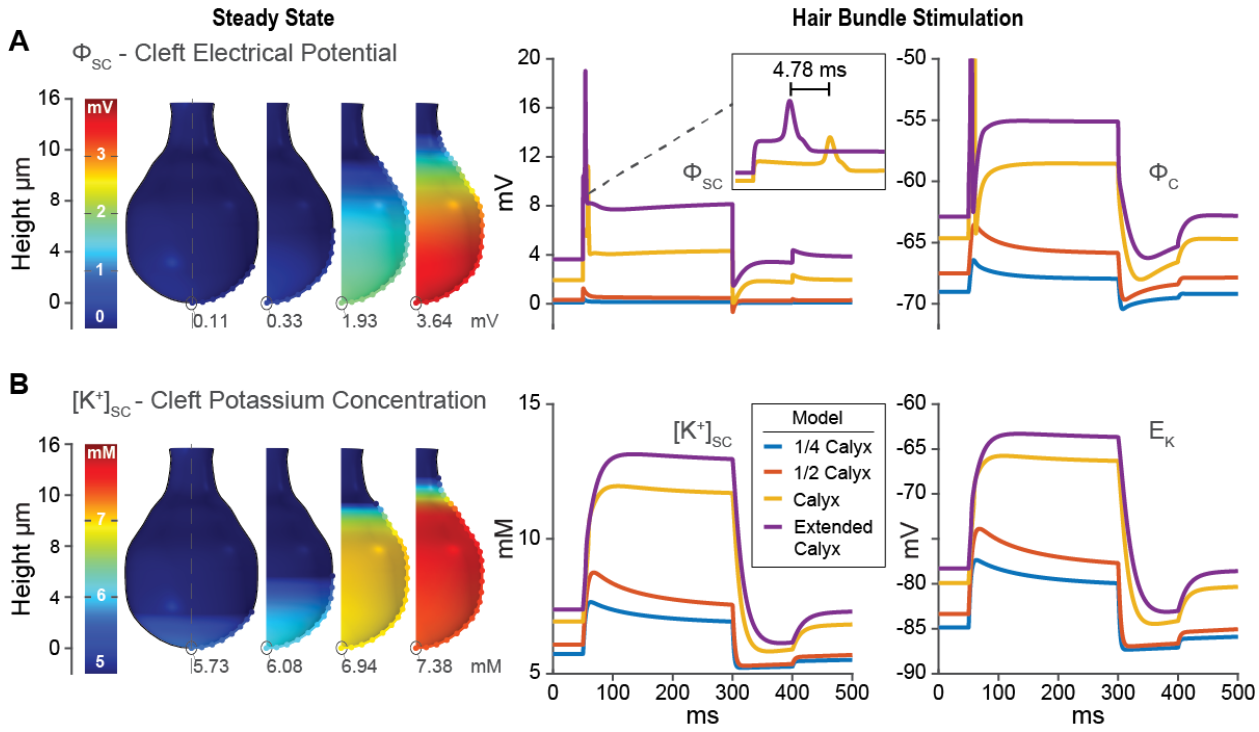

Fig. 7 – Magnitude and speed of nonquantal transmission depend on calyx height.
A, The spatial distribution of ϕ_{SC}at rest (left) and ϕ_{SC} at the base of the synapse (middle) over the course of step bundle displacement (same as in Fig. 1A). Changes in ϕ_{SC} increase in magnitude as a function of calyx height. The inset demonstrates the reduction in time to spike as calyx height is increased by 2 μm from 11.3 to 13.3 μm. Corresponding changes in ϕ_C (right).
B, The spatial distribution of $[K^+]_{SC}$ at rest (left) and $[K^+]_{SC}$ over the course of step bundle displacement at the base of the synapse (middle). Changes in $[K^+]_{SC}$ are larger in magnitude as the calyx is extended. Corresponding E_K values (right). In **A, B, Left,** Small colored frills mark the extent of the synaptic cleft for calyces of different heights and spatial gradients of ϕ_{SC} and $[K^+]_{SC}$ are visible within these regions. The outer surface of the hair cell above the calyx is exposed to perilymph and is at values of 0 mV and 5 mM for electrical potential and potassium concentration respectively.

Discussion

We have constructed a biophysical model that incorporates ultrastructural data on the geometry of the VHCC synapse, immunocytochemical data on the expression of ion channels and transporters and electrophysiological data on kinetics of ion channels. Our goal was to test our intuitions that NQT depends on two outstanding features of this synapse: the extensive thin synaptic cleft, and the many low-voltage-activated potassium (K_{LV}) channels populating membranes on both sides of the cleft. The model enables the prediction of experimentally inaccessible parameters, including potassium concentration $[K^+]_{SC}$ and electrical potential ϕ_{SC} in the synaptic cleft. The model also enables us to simulate dynamic changes in these parameters in response to hair bundle deflection and paired voltage clamp recordings and make quantitative predictions that align with experimental recordings.

The VHCC model permits a clear description of the sequence of biophysical events that give rise to NQT, as summarized in **Fig. 8**. Modulation of hair cell potential immediately changes the synaptic cleft potential ϕ_{SC} and more gradually changes the potassium potential E_K. Both processes are initiated by a large K^+ current through the non-inactivating, low-voltage-activated potassium conductance, $g_{K,L}$, on the hair cell basolateral membrane. The properties of $g_{K,L}$ suit it for its role in NQT. First, $g_{K,L}$ is >50% open at the hair cell resting potential, allowing the receptor potential to immediately change membrane current and thereby ϕ_{SC}. Second, $g_{K,L}$ is non-inactivating, ensuring that significant K^+ will accumulate in the cleft during sustained or low-frequency hair cell stimulation. The changes in cleft electrical and K^+ potentials alter the driving forces on capacitive and resistive currents across the calyx inner face. The calyx inner face bears a large number of different (Kv7) low-voltage-activated channels, which are also significantly open at rest (~30%). K^+ currents through K_V7 channels typically flow into the cleft but depolarization of ϕ_{SC} and K^+ accumulation in the cleft reduces the outward current and depolarizes the calyx. The presence of open K_{LV} channels in the membranes facing each other across the cleft enables fast non-quantal transmission.

What naturally emerges from the VHCC model is that changes in ϕ_{SC} and $[K^+]_{SC}$ are complementary mechanisms that work together to produce NQT. The near-instantaneous change in ϕ_{SC} enables the calyx to closely follow changes in hair cell potential. This explains the short latency of the NQ response observed experimentally (Songer and Eatock 2013; Contini et al. 2020) and ultimately enables afferent neurons to frequency-follow at relatively high frequencies (Songer and Eatock 2013). The slower changes in $[K^+]_{SC}$ increase the gain of NQT for slow or sustained hair bundle deflections. The model also demonstrates that

the calyx geometry is essential for both fast and slow NQT; as calyx height increases, ϕ_{SC} and $[K^+]_{SC}$ increase and transmission latency decreases.

These predictions provide a biophysical basis for the exceptional speed of neurotransmission between type I hair cells and vestibular afferents, which is even faster than the quantal transmission between cochlear hair cells and afferents (McCue and Guinan 1994). At its fastest, quantal transmission imposes a 0.3-0.4-ms delay (McCue and Guinan 1994), reflecting the time required for multiple steps from the opening of presynaptic voltage-gated calcium channels to the opening of postsynaptic neurotransmitter-gated receptor channels. For vestibular reflexes, with latencies as short as 5 ms (Huterer and Cullen 2002), shaving off the quantal transmission delay of the first synapse in the pathway is significant. Our results suggest that robust NQT, enabled by the evolution of the full calyx, substantially increases the speed of vestibular reflexes.

While changes in $[K^+]_{SC}$ were previously postulated (Goldberg 1996) and supported by experimental data (Lim et al. 2011), the VHCC model predicts that changes in ϕ_{SC} are also necessary to account for experimental observations, especially the speed of NQT. The role of electrical potential was considered in an earlier model of nonquantal transmission (Goldberg, 1996) but thought to be insignificant. At that time, it was known that the type I hair cell has a large K^+ conductance, $g_{K,L}$, that is open at resting potential (Correia and Lang 1990; Rennie and Correia 1994; Rüsch and Eatock 1996), but there was almost no information about calyceal ion channels and as a result, the postsynaptic membrane resistance was incorrectly assumed to be high. Since then, whole-cell patch clamp recordings have provided indirect evidence for K^+ accumulation in the cleft (Lim et al. 2011; Contini et al. 2012, 2017, 2020) and studies have identified an abundance of low-voltage-activated K_V1 and K_V7 channels in the calyx inner-face membrane (Hurley et al. 2006; Sousa et al. 2009; Lysakowski et al. 2011; Songer and Eatock 2013; Spitzmaul et al. 2013; Holt et al. 2017).

The effect of K_{LV} channels to reduce membrane charging time and expand the frequency bandwidth of type I hair cells has been noted previously (Rennie et al. 1996; Rüsch and Eatock 1996; Songer and Eatock 2013). These channels were at first considered problematic as they would interfere with robust quantal transmission (Bao et al. 2003; Holt et al. 2007) by (1) polarizing the hair cell membrane negative to the activation range of voltage-gated calcium (Ca_V) currents that mediate quantal transmission, and (2) attenuating the voltage changes that drive quantal transmission. During prolonged (250 ms) excitatory hair bundle deflections, however, our simulations show that currents through $g_{K,L}$ on the hair cell and K_V7

channels on the calyx inner face permit NQT by mediating significant changes in ϕ_{SC} and $[K^+]_{SC}$ and lead to significant depolarization of the hair cell (15-20 mV) and calyx (5-10 mV). It has been further proposed that by depolarizing cleft E_K and therefore the pre- and post-synaptic membranes, NQT aids vesicle release from type I hair cells (Chen 1995; Goldberg 1996; Contini et al. 2017). Indeed, at the type I-calyx synapse in turtles, NQT depolarizes the hair cell membrane into the activation range of Ca_V channels that mediate quantal transmission (Contini et al. 2017).

In conclusion, the VHCC model quantifies two parallel mechanisms of NQT — changes in the cleft electrical potential, ϕ_{SC}, and potassium concentration, $[K^+]_{SC}$ — and delineates the roles of specific ion channels and calyx geometry. Here we have focused on a simple calyx from central or striolar zones of vestibular epithelia; the model can be extended to explore the functional impacts of such variations as the complex calyces that enwrap multiple type I hair cells and the elaborate dimorphic terminal arbors that include calyces and boutons. While the VHCC model has been developed for vestibular synapses, similar biophysical mechanisms may augment transmission at other large or enclosed synaptic clefts in the nervous system.

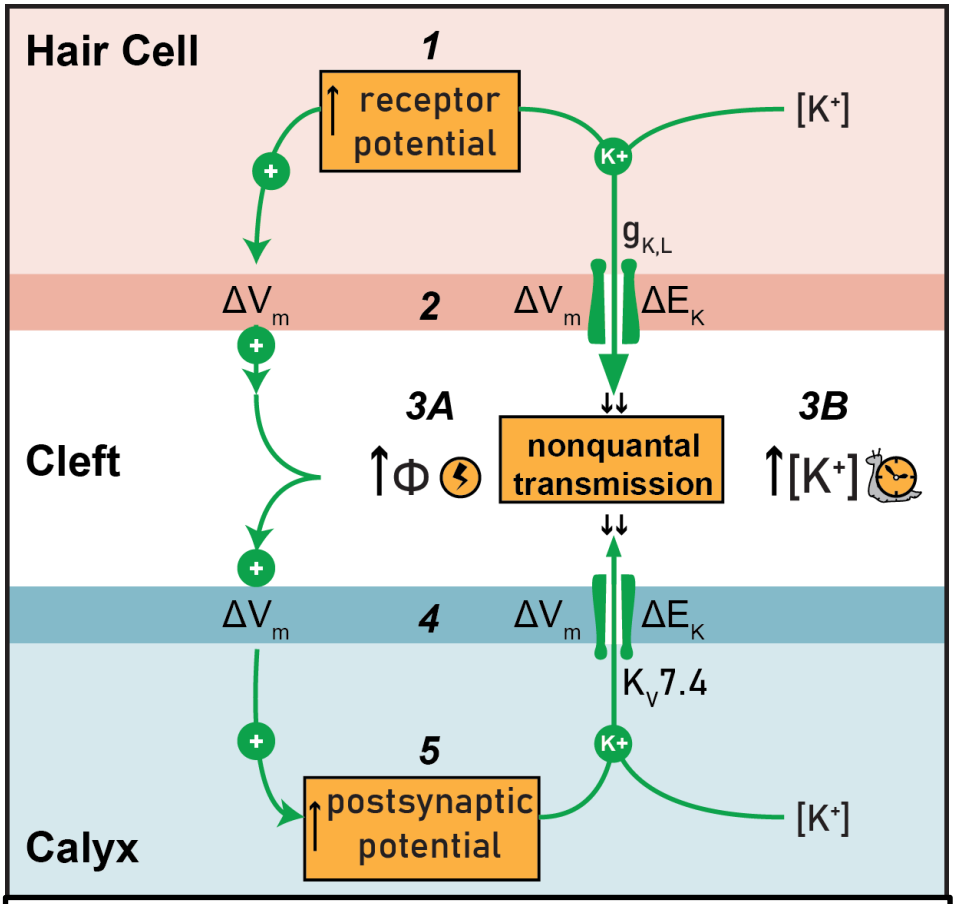

Fig. 8 – Nonquantal Transmission

1. Depolarizing receptor potential due to positive bundle deflection.
2. Change in hair cell membrane voltage drives capacitive currents and *increases* outward resistive current through $g_{K,L}$.
3. Changes in the synaptic cleft
   a. Fast rise in potential in the synaptic cleft, ϕ_{SC}
   b. Gradual rise in cleft potassium concentration $[K^+]_{SC}$
4. Changes in ϕ_{SC} and $[K^+]_{SC}$ alter membrane voltage and E_K respectively across the calyx inner face. This drives capacitive currents and *decreases* outward resistive current through $K_V7.4$
5. The postsynaptic potential depolarizes (Calyx is depolarized). Note that the cleft compartmentalizes the calyx membrane into inner and outer faces, with different trans-membrane voltages. The postsynaptic potential corresponds to that measured with respect to perilymph and across the calyx outer face.

Data Availability

The model was implemented in Comsol Multiphysics 5.6 software. Equations and data sources are available in **SI Computational Methods and Experimental Methods.**

Author Contributions:

RAE and RMR conceived and supervised the work. ACG expanded an initial model developed by IQ. ACG and IQ wrote COMSOL and Matlab code for model implementation. RAE and AL supervised the acquisition of data presented in the Supplement. The manuscript was written by ACG, RMR and RAE and revised and edited by all authors.

Acknowledgements

This study was supported by National Institutes of Health (R01 DC012347 and DC002290) and a seed grant from the RICE ENRICH program. We are grateful to Hannah Martin for stimulating discussions and Selina Baeza-Loya for providing activation and inactivation time constants of afferent voltage-gated sodium channels.

References

Bao H, **Wong WH**, **Goldberg JM**, **Eatock RA**. Voltage-gated calcium channel currents in type I and type II hair cells isolated from the rat crista. *J Neurophysiol* 90: 155–164, 2003.

Baumann SB, **Wozny DR**, **Kelly SK**, **Meno FM**. The electrical conductivity of human cerebrospinal fluid at body temperature. *IEEE Trans Biomed Eng* 44: 220–223, 1997.

Bezanilla F. Single sodium channels from the squid giant axon. *Biophys J* 52: 1087–1090, 1987.

Boyle R, **Ehsanian R**, **Mofrad A**, **Popova Y**, **Varelas J**. Morphology of the utricular otolith organ in the toadfish, *Opsanus tau*. *J Comp Neurol* 526: 1571–1588, 2018.

Chabbert C, **Chambard JM**, **Sans A**, **Desmadryl G**. Three types of depolarization-activated potassium currents in acutely isolated mouse vestibular neurons. *J Neurophysiol* 85: 1017–1026, 2001.

Chen JWY. The properties and functions of a low-voltage activated potassium ion current in type I hair cells of rat semicircular canal organs. *ProQuest Dissertations and Theses* University of Rochester, 1995.

Chen JWY, **Eatock RA**. Major potassium conductance in type I hair cells from rat semicircular canals: characterization and modulation by nitric oxide. *J Neurophysiol* 84: 139–151, 2000.

Chiang C, **Shivacharan RS**, **Wei X**, **Gonzalez-Reyes LE**, **Durand DM**. Slow periodic activity in the longitudinal hippocampal slice can self-propagate non-synaptically by a mechanism consistent with ephaptic coupling. *J Physiol* 597: 249–269, 2019.

Colebatch JG, **Rosengren SM**. Investigating short latency subcortical vestibular projections in humans: what have we learned? *J Neurophysiol* 122: 2000–2015, 2019.

Contini D, **Holstein GR**, **Art JJ**. Synaptic cleft microenvironment influences potassium permeation and synaptic transmission in hair cells surrounded by calyx afferents in the turtle. *J Physiol* 598: 853–889, 2020.

Contini D, **Price SD**, **Art JJ**. Accumulation of K^+ in the synaptic cleft modulates activity by influencing both vestibular hair cell and calyx afferent in the turtle. *J Physiol* 595: 777–803, 2017.

Contini D, **Zampini V**, **Tavazzani E**, **Magistretti J**, **Russo G**, **Prigioni I**, **Masetto S**. Intercellular K^+ accumulation depolarizes type I vestibular hair cells and their associated afferent nerve calyx. *Neuroscience* 227: 232–246, 2012.

Corey DP, **Akyuz N**, **Holt JR**. Function and dysfunction of TMC channels in inner ear hair cells. *Cold Spring Harb Perspect Med* 9, 2019.

Corns LF, **Johnson SL**, **Kros CJ**, **Marcotti W**. Calcium entry into stereocilia drives adaptation of the mechanoelectrical transducer current of mammalian cochlear hair cells. *Proc Natl Acad Sci USA* 111: 14918–14923, 2014.

Correia MJ, **Lang DG**. An electrophysiological comparison of solitary type I and type II vestibular hair cells. *Neurosci Lett* 116: 106–111, 1990.

Crambert G, **Hasler U**, **Beggah AT**, **Yu C**, **Modyanov NN**, **Horisberger J-D**, **Lelièvre L**, **Geering K**. Transport and pharmacological properties of nine different human Na,K-ATPase isozymes. *J Biol Chem* 275: 1976–1986, 2000.

Curthoys IS, **Grant JW**, **Pastras CJ**, **Brown DJ**, **Burgess AM**, **Brichta AM**, **Lim R**. A review of mechanical and synaptic processes in otolith transduction of sound and vibration for clinical VEMP testing. *J Neurophysiol* 122: 259–276, 2019.

Curtis HJ, **Cole KS**. Transverse electric impedance of the squid giant axon. *J Gen Physiol* 21: 757–765, 1938.

Dalet A, **Bonsacquet J**, **Gaboyard-Niay S**, **Calin-Jageman I**, **Chidavaenzi RL**, **Venteo S**, **Desmadryl G**, **Goldberg JM**, **Lysakowski A**, **Chabbert C**. Glutamate transporters EAAT4 and EAAT5 are expressed in vestibular hair cells and calyx endings. *PLoS ONE* 7: e46261, 2012.

Desai SS, **Ali H**, **Lysakowski A**. Comparative morphology of rodent vestibular periphery. II. cristae ampullares. *J Neurophysiol* 93: 267–280, 2005a.

Desai SS, **Zeh C**, **Lysakowski A**. Comparative morphology of rodent vestibular periphery. I. Saccular and utricular maculae. *J Neurophysiol* 93: 251–266, 2005b.

Eatock RA. Specializations for fast signaling in the amniote vestibular inner ear. *Integr Comp Biol* 58: 341–350, 2018.

Freeman SA, **Desmazières A**, **Fricker D**, **Lubetzki C**, **Sol-Foulon N**. Mechanisms of sodium channel clustering and its influence on axonal impulse conduction. *Cell Mol Life Sci* 73: 723–735, 2016.

Geddes LA, **Baker LE**. The specific resistance of biological material--a compendium of data for the biomedical engineer and physiologist. *Med Biol Eng* 5: 271–293, 1967.

Gentet LJ, **Stuart GJ**, **Clements JD**. Direct measurement of specific membrane capacitance in neurons. *Biophys J* 79: 314–320, 2000.

Ginzberg RD. Freeze-fracture morphology of the vestibular hair cell-primary afferent synapse in the chick. *J Neurocytol* 13: 393–405, 1984.

Goldberg JM. Theoretical analysis of intercellular communication between the vestibular type I hair cell and its calyx ending. *J Neurophysiol* 76: 1942–1957, 1996.

Gulley RL, **Bagger-Sjöbäck D**. Freeze-fracture studies on the synapse between the type I hair cell and the calyceal terminal in the guinea-pig vestibular system. *J Neurocytol* 8: 591–603, 1979.

Highstein SM, **Holstein GR**, **Mann MA**, **Rabbitt RD**. Evidence that protons act as neurotransmitters at vestibular hair cell–calyx afferent synapses. *Proc Natl Acad Sci USA* 111: 5421–5426, 2014.

Hoffman LF, **Honrubia V**. Fiber diameter distributions in the chinchilla's ampullary nerves. *Hear Res* 172: 37–52, 2002.

Holt JC, **Chatlani S**, **Lysakowski A**, **Goldberg JM**. Quantal and nonquantal transmission in calyx-bearing fibers of the turtle posterior crista. *J Neurophysiol* 98: 1083–1101, 2007.

Holt JC, **Jordan PM**, **Lysakowski A**, **Shah A**, **Barsz K**, **Contini D**. Muscarinic acetylcholine receptors and M-currents underlie efferent-mediated slow excitation in calyx-bearing vestibular afferents. *J Neurosci* 37: 1873–1887, 2017.

Holt JR, **Corey DP**, **Eatock RA**. Mechanoelectrical transduction and adaptation in hair cells of the mouse utricle, a low-frequency vestibular organ. *J Neurosci* 17: 8739–8748, 1997.

Honrubia V, **Hoffman LF**, **Sitko S**, **Schwartz IR**. Anatomic and physiological correlates in bullfrog vestibular nerve. *J Neurophysiol* 61: 688–701, 1989.

Horwitz GC, **Risner-Janiczek JR**, **Holt JR**. Mechanotransduction and hyperpolarization-activated currents contribute to spontaneous activity in mouse vestibular ganglion neurons. *J Gen Physiol* 143: 481–497, 2014.

Horwitz GC, **Risner-Janiczek JR**, **Jones SM**, **Holt JR**. HCN channels expressed in the inner ear are necessary for normal balance function. *J Neurosci* 31: 16814–16825, 2011.

Hurley KM, **Gaboyard S**, **Zhong M**, **Price SD**, **Wooltorton JRA**, **Lysakowski A**, **Eatock RA**. M-like K^+ currents in type I hair cells and calyx afferent endings of the developing rat utricle. *J Neurosci* 26: 10253–10269, 2006.

Huterer M, **Cullen KE**. Vestibuloocular reflex dynamics during high-frequency and high-acceleration rotations of the head on body in rhesus monkey. *J Neurophysiol* 88: 13–28, 2002.

Jaisser F, **Jaunin P**, **Geering K**, **Rossier BC**, **Horisberger JD**. Modulation of the Na,K-pump function by beta subunit isoforms. *J Gen Physiol* 103: 605–623, 1994.

Kalluri R, **Xue J**, **Eatock RA**. Ion channels set spike timing regularity of mammalian vestibular afferent neurons. *J Neurophysiol* 104: 2034–2051, 2010.

Kay AR, **Sugimori M**, **Llinás R**. Kinetic and stochastic properties of a persistent sodium current in mature guinea pig cerebellar Purkinje cells. *J Neurophysiol* 80: 1167–1179, 1998.

Köppl C, **Wilms V**, **Russell IJ**, **Nothwang HG**. Evolution of endolymph secretion and endolymphatic potential generation in the vertebrate inner ear. *Brain Behav Evol* 92: 1–31, 2018.

Lanford PJ, **Popper AN**. Novel afferent terminal structure in the crista ampullaris of the goldfish, carassius auratus. *J Comp Neurol* 366: 572–579, 1996.

Lee C-H, **MacKinnon R**. Structures of the human HCN1 hyperpolarization-activated channel. *Cell* 168: 111-120.e11, 2017.

Li Y, **Liu H**, **Zhao X**, **He DZ**. Endolymphatic potential measured from developing and adult mouse inner ear. *Front Cell Neurosci* 14: 584928–584928, 2020.

Lide DR, **Baysinger G**, **Berger LI**, **Goldberg RN**, **Kehiaian HV**, **Kuchitsu K**, **Rosenblatt G**, **Roth DL**, **Zwillinger D**, editors. CRC Handbook of Chemistry and Physics [Online]. 85th ed. CRC Press. http://www.hbcpnetbase.com.

Lim R, **Kindig AE**, **Donne SW**, **Callister RJ**, **Brichta AM**. Potassium accumulation between type I hair cells and calyx terminals in mouse crista. *Exp Brain Res* 210: 607–621, 2011.

Liu X-P, **Wooltorton JRA**, **Gaboyard-Niay S**, **Yang F-C**, **Lysakowski A**, **Eatock RA**. Sodium channel diversity in the vestibular ganglion: Na_V 1.5, Na_V 1.8, and tetrodotoxin-sensitive currents. *J Neurophysiol* 115: 2536–2555, 2016.

Lysakowski A, **Gaboyard-Niay S**, **Calin-Jageman I**, **Chatlani S**, **Price SD**, **Eatock RA**. Molecular microdomains in a sensory terminal, the vestibular calyx ending. *J Neurosci* 31: 10101–10114, 2011.

Lysakowski A, **Goldberg JM**. A regional ultrastructural analysis of the cellular and synaptic architecture in the chinchilla cristae ampullares. *J Comp Neurol* 389: 419–443, 1997.

Lysakowski A, **Goldberg JM**. Morphophysiology of the vestibular periphery. In: *The Vestibular System*, edited by Highstein SM, Fay RR, Popper AN. Springer New York, p. 57–152.

Lysakowski A, **Goldberg JM**. Ultrastructural analysis of the cristae ampullares in the squirrel monkey (Saimiri sciureus). *J Comp Neurol* 511: 47–64, 2008.

Marcoux AA, **Garneau AP**, **Frenette-Cotton R**, **Slimani S**, **Mac-Way F**, **Isenring P**. Molecular features and physiological roles of K^+ - Cl^- cotransporter 4 (KCC4). *Biochim Biophys Acta (BBA)* 1861: 3154–3166, 2017.

McCue M, **Guinan J**. Acoustically responsive fibers in the vestibular nerve of the cat. *J Neurosci* 14: 6058–6070, 1994.

Mercado A, **Song L**, **Vázquez N**, **Mount DB**, **Gamba G**. Functional comparison of the K^+-Cl^- cotransporters KCC1 and KCC4. *J Biol Chem* 275: 30326–30334, 2000.

Meredith FL, **Rennie KJ**. Zonal variations in K^+ currents in vestibular crista calyx terminals. *J Neurophysiol* 113: 264–276, 2015.

Meredith FL, **Rennie KJ**. Regional and developmental differences in Na^+ currents in vestibular primary afferent neurons. *Front Cell Neurosci* 12, 2018.

Nicholson C, **Phillips JM**. Ion diffusion modified by tortuosity and volume fraction in the extracellular microenvironment of the rat cerebellum. *J Physiol* 321: 225–257, 1981.

Rennie KJ, **Correia MJ**. Potassium currents in mammalian and avian isolated type I semicircular canal hair cells. *J Neurophysiol* 71: 317–329, 1994.

Rennie KJ, **Ricci AJ**, **Correia MJ**. Electrical filtering in gerbil isolated type I semicircular canal hair cells. *J Neurophysiol* 75: 2117–2123, 1996.

Ritchie JM, **Rogart RB**. Density of sodium channels in mammalian myelinated nerve fibers and nature of the axonal membrane under the myelin sheath. *Proc Natl Acad Sci USA* 74: 211–215, 1977.

Rüsch A, **Eatock RA**. A delayed rectifier conductance in type I hair cells of the mouse utricle. *J Neurophysiol* 76: 995–1004, 1996.

Sadeghi SG, **Pyott SJ**, **Yu Z**, **Glowatzki E**. Glutamatergic signaling at the vestibular hair cell calyx synapse. *J Neurosci* 34: 14536–14550, 2014.

Schuth O, **McLean WJ**, **Eatock RA**, **Pyott SJ**. Distribution of Na,K-ATPase α subunits in rat vestibular sensory epithelia. *J Assoc Res Otolaryngol* 15: 739–754, 2014.

Songer JE, **Eatock RA**. Tuning and timing in mammalian type I hair cells and calyceal synapses. *J Neurosci* 33: 3706–3724, 2013.

Soto E, **Vega R**, **Budelli R**. The receptor potential in type I and type II vestibular system hair cells: a model analysis. *Hear Res* 165: 35–47, 2002.

Sousa AD, **Andrade LR**, **Salles FT**, **Pillai AM**, **Buttermore ED**, **Bhat MA**, **Kachar B**. The septate junction protein Caspr is required for structural support and retention of KCNQ4 at calyceal synapses of vestibular hair cells. *J Neurosci* 29: 3103–3108, 2009.

Spaiardi P, **Tavazzani E**, **Manca M**, **Milesi V**, **Russo G**, **Prigioni I**, **Marcotti W**, **Magistretti J**, **Masetto S**. An allosteric gating model recapitulates the biophysical properties of $I_{K,L}$ expressed in mouse vestibular type I hair cells: Allosteric gating of $I_{K,L}$. *J Physiol* 595: 6735–6750, 2017.

Spaiardi P, **Tavazzani E**, **Manca M**, **Russo G**, **Prigioni I**, **Biella G**, **Giunta R**, **Johnson SL**, **Marcotti W**, **Masetto S**. K^+ accumulation and clearance in the calyx synaptic cleft of type I mouse vestibular hair cells. *Neuroscience* 426: 69–86, 2020.

Spitzmaul G, **Tolosa L**, **Winkelman BHJ**, **Heidenreich M**, **Frens MA**, **Chabbert C**, **de Zeeuw CI**, **Jentsch TJ**. Vestibular role of KCNQ4 and KCNQ5 K^+ channels revealed by mouse models. *J Biol Chem* 288: 9334–9344, 2013.

Stämpfli R. Saltatory conduction in nerve. *Physiol Rev* 34: 101–112, 1954.

Ventura CM, **Kalluri R**. Enhanced activation of HCN channels reduces excitability and spike-timing regularity in maturing vestibular afferent neurons. *J Neurosci* 1811–18, 2019.

Vroman R, **Klaassen LJ**, **Kamermans M**. Ephaptic communication in the vertebrate retina. *Front Hum Neurosci* 7: 612, 2013.

Wang K, **Zhao Y**, **Chen D**, **Fan B**, **Lu Y**, **Chen L**, **Long R**, **Wang J**, **Chen J**. Specific membrane capacitance, cytoplasm conductivity and instantaneous Young's modulus of single tumour cells. *Scientific Data* 4: 170015, 2017.

Warren TJ, **Van Hook MJ**, **Tranchina D**, **Thoreson WB**. Kinetics of inhibitory feedback from horizontal cells to photoreceptors: implications for an ephaptic mechanism. *J Neurosci* 36: 10075–10088, 2016.

Wong WH, **Hurley KM**, **Eatock RA**. Differences between the negatively activating potassium conductances of mammalian cochlear and vestibular hair cells. *J Assoc Res Otolaryngol* 5: 270–284, 2004.

Yamashita M, **Ohmori H**. Synaptic responses to mechanical stimulation in calyceal and bouton type vestibular afferents studied in an isolated preparation of semicircular canal ampullae of chicken. *Exp Brain Res* 80: 475–488, 1990.

Yamashita M, **Ohmori H**. Synaptic bodies and vesicles in the calix type synapse of chicken semicircular canal ampullae. *Neurosci Lett* 129: 43–46, 1991.

Zhou T, **Ming Y**, **Perry SF**, **Tatic-Lucic S**. Estimation of the physical properties of neurons and glial cells using dielectrophoresis crossover frequency. *J Biol Phys* 42: 571–586, 2016.

Supplementary Information

Computational Methods

Overview. The Vestibular Hair-Cell Calyx (VHCC) model incorporates information on synapse morphology, ion transporters and ion channels expressed in type I hair cells (transduction channels, K_V channels, Ca_V channels, HCN channels, Na^+/K^+-ATPase), and in calyces and afferent fibers (K_V, Na_V channels, HCN channels, KCC, Na^+/K^+-ATPase) (see **Fig. 1** in main text). The dynamic behavior of the system is determined from measured or estimated channel open probabilities, time constants and whole-cell conductances, and from assumptions (which we describe) about the activity of ion transporters based on literature. We implemented the VHCC model with finite-element-analysis simulation software, using equations for K^+ and Na^+ electro-diffusion in the cleft, Hodgkin-Huxley-style equations to represent voltage-dependent ion flow through ion channels, and the cable equation for electrical propagation. For each simulation, steady-state conditions are established and followed by a step or sinusoidal deflection of the hair bundle or voltage step; outputs include the gradients within the synaptic cleft for K^+, Na^+ and electrical potential, and voltage across the hair-cell-facing postsynaptic membrane of the calyx ("calyx inner face"), and in the hemi-node and first two full nodes of the distal branch of the bipolar vestibular afferent neuron; the distal branch connects the synaptic terminals on hair cells (in this case a single calyx) to the neuronal cell body in the vestibular ganglion. The remainder of the distal branch, the cell body and the central branch projecting to the brain are not included in the model. Negative currents represent the flow of cations into the compartment bearing the channel or transporter in its membrane. The hair cell is assumed to be equipotential based on its small overall size, compact form and low intracellular resistance. Details of model development are described below.

Model Geometry. The model was designed with the COMSOL Multiphysics 5.6 software package. We used a 2D axisymmetric finite element boundary to represent the hair cell, synaptic cleft, and afferent calyx and a 1D finite element line to represent the afferent fiber (**Fig. S1**). The 2D boundary used to represent the hair cell (H), synaptic cleft (SC), the calyx inner face (CIF) and calyx outer face (COF) is an interpolation curve generated from (R,Z) coordinates of the perimeter of a central-zone hair cell and calyx from the central zone of the sensory epithelium of a crista in an adult Long-Evans rat (shown in Fig. 2C of Lysakowski et al. 2011; similar calyces from the striolar zone of the rat utricle are shown in our **Fig. 1A**).

The dimensions and interpolated points used to create the representative geometry in Comsol 5.6 are shown in **Fig. S1.** HN, N and M indicate the hemi-node, nodes and myelinated sections (inter-nodes) of the afferent fiber, respectively. In both 2D (hair cell and calyx) and 1D (fiber) geometries, local properties such as individual channel conductance density, time constants, and steady state expressions for channel gating variables were defined. Note that the apex of the calyx occurred at 11.3 μm for all simulations in the manuscript, except for the variations in calyx height presented in **Fig. 7**.

Finite Element Mesh in Comsol

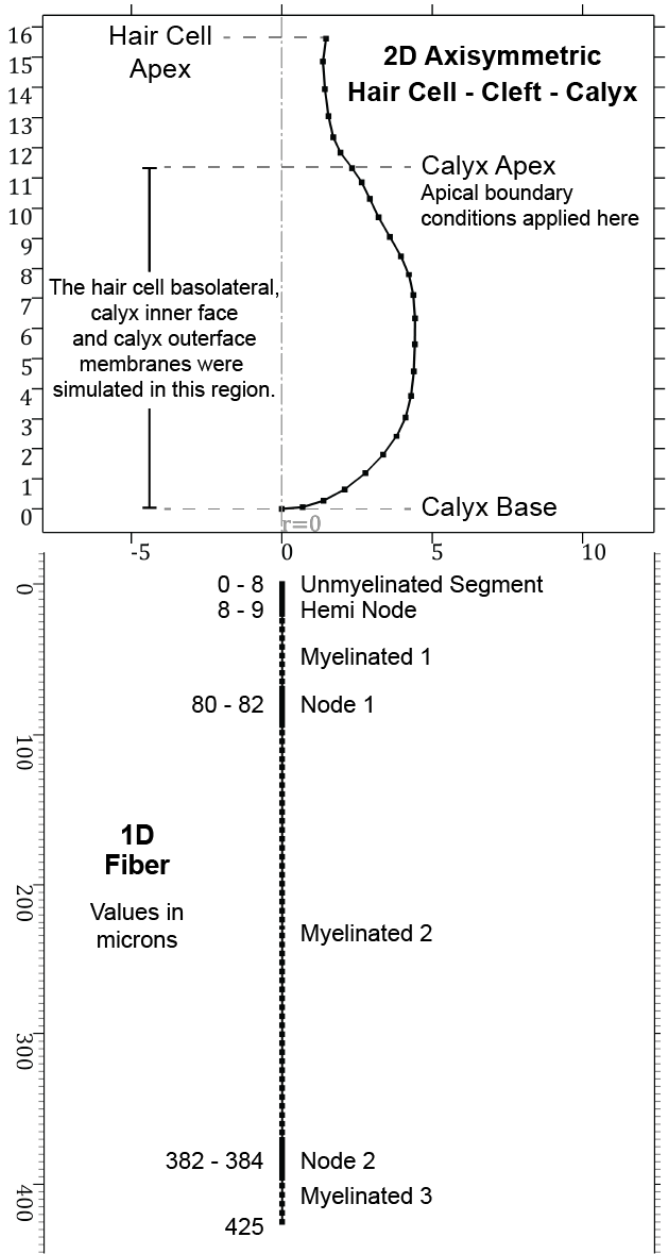

Geometric Parameters

Hair-Cell-Calyx Geometry Interpolation Points	
R (μm)	**Z (μm)**
1.47	15.61 (Hair-Cell Apex)
1.39	14.33
1.5	13.44
1.61	12.72
1.89	11.94
2.33	11.33 (Calyx Apex)
3.16	9.8
4.03	8.28
4.42	5.24
4.03	2.83
2.56	1
1.72	0.43
0	0 (Calyx Base)

Calculated Areas	Values
a_H	340.21 μm^2
$a_{H,C}$	294.63 μm^2
a_{CIF}	294.63 μm^2
a_{COF}	288.33 μm^2
$a_{F,HN}$	3π μm^2
$a_{F,N}$	6π μm^2
$a_{F,Unmyel}$	24π μm^2

Cleft width (d_{SC})	0.02 μm
Calyx width (d_C)	1 μm
Fiber Radius (r_F)	1.5 μm

Fig. S1 – Hair-Cell-Calyx and Fiber Geometries in the COMSOL 5.6 GUI.

The 2D axisymmetric mesh representing the hair cell, synaptic cleft and calyx (top) was modelled based on the geometry of a type I hair-cell-calyx synapse from central/striolar zones of rodent vestibular organs. Dots in the above geometry represent finite element nodes, and lines represent connecting edge elements. The interpolation points were based upon the geometry of a hair cell (measured from background fluorescence) and calyx reported in Fig. 2C of Lysakowski et al. (2011). d_C was obtained from the same calyx. d_{SC} was obtained from Spoendlin (1966). The fiber radius (r_f) is based on (Lysakowski et al. 1995; Hoffman and Honrubia 2002). The fiber end was treated as a closed boundary. Location of the hemi-node and the first node were estimated from micrographs (Lysakowski et al. 2011). $a_{H,C}$ denotes the surface area of the hair cell within the calyx.

Table S1 - Abbreviations

$\boldsymbol{H, C, SC, CIF, COF, F}$	Subscripts denote the hair cell (*H*), calyx (*C*), synaptic cleft (*SC*), calyx inner face (*CIF*), calyx outer face (*COF*) and fiber (*F*) respectively.
$\boldsymbol{\phi_H, , \phi_C, \phi_{SC}, \phi_F}$	Electrical potential in the hair cell, calyx, synaptic cleft and fiber respectively.
$\boldsymbol{\rho_F}$	Resistivity of the afferent fiber. $1/\sigma_F$
$\boldsymbol{[K^+]_{SC}, [Na^+]_{SC}}$	K^+, Na^+ concentrations in the synaptic cleft
$\boldsymbol{c_H}$	Total hair cell capacitance
$\boldsymbol{C_m}$	Specific membrane capacitance.
$\boldsymbol{Ca_V, K_V, Na_V}$	Voltage gated calcium, potassium and sodium channels
$\boldsymbol{D_K, D_{Na}}$	Effective diffusion coefficients for K^+, Na^+ in the synaptic cleft
$\boldsymbol{d_{SC}}$	Width of the synaptic cleft
$\boldsymbol{g_{x,max}}$	Maximum whole-cell conductance of specific channel type
$\boldsymbol{G_{x,max}}$	Maximum conductance density of specific channel type
$\boldsymbol{g_{K,L}}$	Low-voltage-activated potassium conductance of type I hair cells
$\boldsymbol{HCN}$	Hyperpolarization-activated nucleotide-gated (channels)
$\boldsymbol{I_{MET}}$	Mechanotransduction current
$\boldsymbol{J_x}$	Current density through channel or transporter 'x'
J_{M_x}	Current density through membrane 'x'
$\boldsymbol{KCC}$	Potassium Chloride Cotransporter
$\boldsymbol{K_V7}$	Voltage-gated potassium channels formed by subunits encoded by the KCNQ gene family
$\boldsymbol{P_{open}}$	Channel open probability
$\boldsymbol{VHCC}$	Vestibular Hair Cell-Calyx
$\boldsymbol{V_m}$	Membrane voltage

Table S2 – Equilibrium Potentials and Voltages in Respective Compartments

Property			Hair Cell (H)	Syn. Cleft (SC)	Calyx inner face (CIF)	Calyx outer face (COF)	Fiber (F) HN|N|M
E_K	K^+ Equilibrium Potential	mV	$26 \cdot ln(\frac{[K^+]_{SC}}{150})$	-	$26 \cdot ln(\frac{[K^+]_{SC}}{150})$	$26 \cdot ln\left(\frac{5}{150}\right) = -88.4$	-88.4
E_{Na}	Na^+ Equilibrium Potential	mV	$26 \cdot ln\left(\frac{[Na^+]_{SC}}{12}\right)$	-	$26 \cdot ln\left(\frac{[Na^+]_{SC}}{12}\right)$	$26 \cdot ln\left(\frac{140}{12}\right) = 63.8$	63.8
V_m	Membrane Voltage	mV	$\phi_H - \phi_{SC}$	-	$\phi_C - \phi_{SC}$	ϕ_C	ϕ_F

General Modeling of Membrane Currents

Membrane channels and transporters were distributed in the various compartments based on experimental observations (**Table S6, S7**). Abbreviations used for ion channels and other parameters are listed in **Table S1**. For each type of ion, local current density through a particular channel type 'x' was described by **Eq. S1**:

$$J_{ion,x} = G_{x,max} \cdot P_{x,open} \cdot (V_m - E_{ion}) \quad \text{(S1)}$$

$G_{x,max}$ is the maximum conductance density through a channel 'x' per unit area of membrane, obtained by dividing the maximum whole-cell conductance, $g_{x,max}$, by the surface area of the relevant membrane. $P_{x,open}$, calculated as a function of channel gating variables using the Hodgkin-Huxley formalism, is the percentage of the maximal conductance available. The equations describing the kinetics of channel gating variables as functions of membrane voltage and current densities through each channel type are available in **Table S6**. V_m is the transmembrane potential as defined in **Table S2** for each membrane in the model. E_{ion} is the equilibrium potential of the ion species across the membrane and is continuously updated as the ion concentration changes in the synaptic cleft. In the notation for current densities, K, Na, O, indicate the potassium, sodium, and other ions such as Ca^{2+} or Cl^-. Current densities and fluxes, J, through channels and transporters were summed to describe the current densities of ionic species across Hair cell (H) and Calyx Inner Face (CIF) or Calyx Outer Face (COF) membranes. The species currents were in turn summed to obtain the total current densities through each membrane (J_{M_H} , $J_{M_{CIF}}$, $J_{M_{COF}}$, J_{M_F}) (**Table S3**).

See **Table S6** for equations of current densities and kinetics for each channel type.

Table S3– Local and Net Current Densities Across Individual Membranes

J_{K_H}	$J_{K,L} + J_{K,HCN1} + J_{K,NaK}$	$J_{Na_{CIF}}$	$J_{Na,HCN2} + J_{Na,NaK}$	J_{M_H}	$J_{K_H} + J_{Na_H} + J_{O_H}$
J_{Na_H}	$J_{Na,HCN1} + J_{Na,NaK}$	$J_{O_{CIF}}$	$-J_{KCC4}$	$J_{M_{CIF}}$	$J_{K_{CIF}} + J_{Na_{CIF}} + J_{O_{CIF}}$
J_{O_H}	J_{Ca}	$J_{K_{COF}}$	$J_{K,HCN2} + J_{K,NaK}$	$J_{M_{COF}}$	$J_{K_{COF}} + J_{Na_{COF}} + J_{Leak}$
$J_{K_{CIF}}$	$J_{K_V7.4} + J_{K_V11.1} + J_{K,HCN2} + J_{K,NaK} + J_{KCC4}$	$J_{Na_{COF}}$	$J_{Na,HCN2} + J_{Na,NaK}$	J_{M_F}	$J_{K_V7.x} + J_{K_V1.x} + J_{K_V3.4} + J_{Na_V1.x}$

Governing Equations

Continuity equations describe the electric potential and ion concentrations in the various compartments.

Hair Cell Electrical Potential (ϕ_H). The time dependence of the hair cell electrical potential is calculated as a function of hair cell capacitance (c_H), mechanotransduction current (I_{MET}), and current across the basolateral membrane:

$$c_H \frac{\partial \phi_H}{\partial t} = -I_{MET} - \int_0^L 2\pi r \left(J_{M_H} - C_m \frac{\partial \phi_{SC}}{\partial t} \right) ds \tag{S2}$$

I_{MET} is calculated according to an instantaneous current-displacement relationship (Holt et al. 1997) and a maximal conductance of 5 nS, based on ~50 transduction channels of ~100-pS single-channel conductance (Corey et al. 2019). We calculated the total capacitance of the hair cell ($c_H = 6.4\, pF$) by multiplying the surface area of the cell by the specific capacitance of the membrane (C_m).

Concentration and Electro-diffusion in the Synaptic Cleft. $[K^+]_{SC}$ and $[Na^+]_{SC}$ were calculated with the Nernst-Planck electro-diffusion equation for each ion:

$$\frac{\partial [K^+]_{SC}}{\partial t} = \nabla \cdot (D_K \nabla [K^+]_{SC}) + \nabla \cdot (D_K \frac{F}{RT} [K^+]_{SC} \nabla \phi_{SC}) + \frac{1}{d_{SC}} \frac{(J_{K_H} + J_{K_{CIF}})}{F} \tag{S3}$$

$$\frac{\partial [Na^+]_{SC}}{\partial t} = \nabla \cdot (D_{Na} \nabla [Na^+]_{SC}) + \nabla \cdot (D_{Na} \frac{F}{RT} [Na^+]_{SC} \nabla \phi_{SC}) + \frac{1}{d_{SC}} \frac{(J_{Na_H} + J_{Na_{CIF}})}{F} \tag{S4}$$

D_K, the effective diffusion coefficient for K^+, is calculated by dividing the diffusion coefficient of K^+ in aqueous solution at 25 $°C$: $1.957 \cdot 10^{-9}\ \frac{m^2}{s}$ (Lide et al. 2005) by the square of the tortuosity coefficient 1.55 (Nicholson and Phillips 1981), $D_K = 0.81 \cdot 10^{-9} \frac{m^2}{s}$. Similarly, $D_{Na} = 0.56 \cdot 10^{-9} \frac{m^2}{s}$. The volume of the synaptic cleft is assumed to be constant and the width (d_{SC}) and length of the synaptic cleft are fixed.

Electrical Potential in the Synaptic Cleft (ϕ_{SC}). At bouton synapses, the electrical potential in the synaptic cleft, ϕ_{SC}, is assumed to be that of the extracellular medium (at reference potential or ground, ~0 mV) because the resistance of the cleft is assumed to be low. At the VHCC synapse, in contrast, the extended synaptic cleft created by the calyx geometry poses an increased resistance and large K^+ currents that flow during transduction may allow a significant cleft potential. ϕ_{SC} was calculated following the law of charge

conservation as a function of the resistive and capacitive currents across both pre-synaptic (hair cell) and post-synaptic (calyx) membranes, as well as electro-diffusion of ions:

$$(2C_m)\frac{d\phi_{SC}}{dt} = C_m\frac{d\phi_H}{dt} + C_m\frac{d\phi_{Calyx}}{dt} + J_H + J_{CIF} + \nabla\cdot(FD_K\nabla[K^+]_{SC})\cdot d_{SC} + \nabla\cdot(FD_{Na}\nabla[Na^+]_{SC})\cdot d_{SC} + \nabla\cdot\left(\left(\sigma_{O\,SC} + \frac{D_K\,[K^+]_{SC}\,F^2}{RT} + \frac{D_{Na}\,[Na^+]_{SC}\,F^2}{RT}\right)\nabla\phi_{SC}\right)\cdot d_{SC} \quad \text{(S5)}$$

At room temperature, $\frac{D_K\,[K^+]_{SC}\,F^2}{RT} + \frac{D_{Na}\,[Na^+]_{SC}\,F^2}{RT}$ ~ 300 - 400 nS/µm when $[K^+]_{SC}$ and $[Na^+]_{SC}$ range between 5-40 and 120-140 mM respectively. The total conductivity contribution from ions ($\sigma_{O\,SC}$) other than K^+ and Na^+ is set equal to 600 nS/µm to be consistent with the 1000 nS/µm used in the calyx and afferent fiber. This value is within the range reported from measurements in tumor cells (Wang et al. 2017), hippocampal neurons (Zhou et al. 2016) and cerebrospinal fluid (Baumann et al. 1997). The diffusion of other ions, e.g., chloride, was not explicitly considered and their concentrations within the synaptic cleft are assumed to be constant and a part of the $\sigma_{O\,SC}$ term.

Electrical Potential in the Calyx (ϕ_C). The electrical potential within the calyx was calculated as a function of the resistive and capacitive currents across both the post-synaptic membrane and the calyx outer face membranes as well as the longitudinal current from the afferent fiber.

$$(2C_m)\frac{d\phi_C}{dt} = C_m\frac{d\phi_{SC}}{dt} + \nabla\cdot(\sigma_C d_C\,\nabla\phi_C) - J_{\mathrm{CIF}} - J_{\mathrm{COF}} - J_F \quad \text{(S6)}$$

The current from the fiber to the calyx, J_F, is equal to $(-\pi\cdot\frac{r_f}{\rho_l}\cdot u_x)$, where r_f the radius of the fiber is 1.5 µm, ρ_l the longitudinal resistivity is 1 MΩ/µm, and u_x is the longitudinal potential gradient within the fiber. The fiber radius used is comparable to diameters reported for calyx afferents (Hoffman and Honrubia 2002).

Electrical Potential in the Afferent Fiber (ϕ_F). To describe the potential in the afferent fiber, ϕ_F, we implemented the cable equation along the 1D line representing the fiber:

$$r_F^2\frac{d^2\phi_F}{dx^2} = 2r_F\rho_l C_m\frac{d\phi_F}{dt} - 2r_F\rho_F J_{M_F} \quad \text{(S7)}$$

Channel gating variables and conductance densities (See **Table S6**) were defined for the hemi-node, nodes and myelinated regions of the fiber as shown in **Fig. 1**. Gating variables for channels present on the fiber were treated similarly to those on the calyx and hair cell.

Initial and Boundary Conditions. Before running the simulation, the initial value of ϕ_H was set at -70 mV, within the normal range of reported resting potentials for rodent type I hair cells (Rennie and Correia 1994; Rennie et al. 1996; Rüsch and Eatock 1996; Chen and Eatock 2000; Lim et al. 2011; Spaiardi et al. 2017). Where necessary, initial values of ϕ_H were varied $\pm$ 10 mV to assist solver convergence. An initial value of 0 mV was used for the potential in the synaptic cleft, ϕ_{SC}. The boundary condition $\phi_{SC} = 0$ mV was applied at the apical end of the synaptic cleft. An initial value of –70 mV was used for ϕ_{Calyx} and ϕ_F, consistent with recorded resting potentials in rodent calyces ranging –60 to –70 mV in (Meredith and Rennie 2015; Sadeghi et al. 2014; Songer and Eatock 2013). The boundary condition $\phi_{Calyx} = \phi_F$ was applied at the base of the calyx and the far end of the fiber was treated as a closed boundary. $[K^+]_{SC}$ and $[Na^+]_{SC}$ were given initial values of 5 mM and 140 mM, respectively, throughout the cleft, based on the external (bath) recording solutions of electrophysiological data referenced in the model and similar to perilymph facing the outer face of the calyx and other extracellular salines. K^+ and Na^+ concentrations were pinned at these values at the apical end of the cleft but were allowed to vary elsewhere within the cleft. To better understand NQT, we altered the initial conditions to independently analyze the contributions of changes in the synaptic cleft in (1) electrical potential and (2) potassium concentration. As described below, this theoretical exercise gave greater insight into the mechanisms of NQ transmission.

Table S4 – Initial and Boundary Conditions

Parameter	Value	Reference
$\phi_{H,init}$	-75 mV	(Correia and Lang 1990; Rennie and Correia 1994; Rennie et al. 1996; Rüsch and Eatock 1996; Chen and Eatock 2000; Lim et al. 2011; Spaiardi et al. 2017)
$\phi_{SC,init}$	0 mV	Based on the external (bath) recording solutions of electrophysiological data referenced in the model
$\phi_{SC,apical}$	0 mV	
$[K^+]_{SC,init}$ $[K^+]_{SC,apical}$	5 mM	
$[Na^+]_{SC,init}$ $[Na^+]_{SC,apical}$	140 mM	
$\phi_{C,init}$	-70 mV	(Meredith and Rennie 2015; Sadeghi et al. 2014; Songer and Eatock 2013)
$\phi_{F,init}$	-70 mV	Assumed continuous with $\phi_{C,init}$

ϕ_{SC}-Only Condition. To isolate the contribution of changes in electrical potential within the synaptic cleft to NQ transmission, we held ion concentrations in the synaptic cleft constant at 5 mM for $[K^+]_{SC}$ and 140 mM $[Na^+]_{SC}$ (**Eqs. S3 and S4**) and removed terms for ion diffusion in the cleft from **Eq. S5**.

$$(2C_m)\frac{d\phi_{SC}}{dt} = C_m\frac{d\phi_H}{dt} + C_m\frac{d\phi_C}{dt} + J_{\mathrm{H}} + J_{\mathrm{CIF}} + \nabla \cdot \left(\left(\sigma_{O_{SC}} + \frac{D_K[K^+]_{SC}F^2}{RT} + \frac{D_{Na}[Na^+]_{SC}F^2}{RT}\right)\nabla\phi_{SC}\right)\cdot d_{SC} \tag{S8}$$

$$\frac{\partial[K^+]_{SC}}{\partial t} = 0\,;\ [K^+]_{SC} = 5\ mM \tag{S9}$$

$$\frac{\partial[Na^+]_{SC}}{\partial t} = 0;\ [Na^+]_{SC} = 140\ mM \tag{S10}$$

$[K^+]_{SC}$-Only Condition. To isolate the contribution of changes in K^+ concentration in the synaptic cleft to NQ transmission, we fixed ϕ_{SC} at 0 mV and removed the electrical drift terms in **Eqs. S3 and S4**.

$$(2C_m)\frac{d\phi_{SC}}{dt} = 0\,;\ \phi_{SC} = 0\ mV \tag{S11}$$

$$\frac{\partial[K^+]_{SC}}{\partial t} = \nabla \cdot (D_K \nabla[K^+]_{SC}) + \frac{1}{d_{SC}} \frac{(J_{K_H} + J_{K_{CIF}})}{F} \tag{S12}$$

$$\frac{\partial[Na^+]_{SC}}{\partial t} = \nabla \cdot (D_{Na} \nabla[Na^+]_{SC}) + \frac{1}{d_{SC}} \frac{(J_{Na_H} + J_{Na_{CIF}})}{F} \tag{S13}$$

Model Simulation and Solver Conditions

In the COMSOL 5.6 software, the finite element mesh was generated based on geometric parameters for the hair-cell-calyx and fiber (**Fig. S1**). The number and distribution of finite element nodes (hair-cell-calyx: 26 nodes, 25 edge elements; fiber: 95 nodes, 94 edge elements) was chosen to minimize error in the solutions of the governing equations. To obtain the resting conditions, we ran the model simulation with a stationary solver. For a step or sinusoidal displacement of the hair cell's stereociliary bundle or hair cell voltage steps, we used a time-dependent solver to determine the responses in the hair cell, synaptic cleft, calyx and afferent fiber. The time-dependent solver was run using the backward difference formula (BDF) method. The temporal resolution (maximum time step) was: 1 ms for resting conditions before stimulus onset; 0.01 ms from 1 ms before stimulus onset to 10 ms after stimulus onset; and 0.1 ms for all other intervals. The model simultaneously solves **Eqs. S1-S7** to simulate the electrical potential of the hair cell and the spatiotemporal evolution of electrical potential, potassium concentration, sodium concentration in the synaptic cleft, and potential in the afferent fiber.

Table S5 – Conductances, Diffusion Coefficients and Capacitances

σ_C	1000 nS/µm	(Baumann et al. 1997; Geddes and Baker 1967; Zhou et al. 2016; Wang et al. 2017)
C_m	0.01 pF/µm^2	(Curtis and Cole 1938; Gentet et al. 2000)
$C_{m,Myel}$	0.00002 pF/µm^2	(Stämpfli 1954)
D_K	0.81 µm/ms	(Lide et al. 2005). See methods near **Eq. S4**
D_{Na}	0.56 µm/ms	(Lide et al. 2005). See methods near **Eq. S4**
$g_{bundle,max}$	5 nS	(Holt et al. 1997)
$g_{Ca,max}$	0.5 nS	(Bao et al. 2003)
$g_{HCN1,max}$	4.2 nS	(Horwitz et al. 2011)
$g_{HCN2,max}$	3.6 nS	(Horwitz et al. 2014)
$g_{K,L,max}$	80 nS	(Spaiardi et al. 2017)
$g_{K_V7.4,max}$	24 nS	(Hurley et al. 2006)
$g_{K_V1.x,max}$	6.3 nS	(Kalluri et al. 2010)
$G_{K_V3.4,max}$	0.2 nS/µm^2	(Chabbert et al. 2001)
$g_{K_V7.x,max}$	4.5 nS	(Kalluri et al. 2010)
$g_{Na_V,unitary}$	10 pS	(Bezanilla 1987; Kay et al. 1998)
ρ_{Na_V}	12,000/µm^2	(Ritchie and Rogart 1977)

Channel Distribution and Kinetics

The governing equations depend upon the net current densities across the pre- and post-synaptic membranes in the model. The constitutive currents and their kinetics as used in the model are detailed in **Table S6**. All channel properties used were from electrophysiological measurements near room temperature (23 – 27°C). For a given channel, $act_{\infty}(V)$ and $\tau_{act}(V)$ are expressions for the dependence of the activation 'act' (or inactivation 'inact') gating variable on the membrane voltage and the corresponding time constant. $act(t)$ is the instantaneous value of the gating variable. The expressions for $act(V)$ and $\tau_{act}(V)$ were stored in variables assigned to the VHCC and fiber geometry to make them locally available during model evaluation. The maximum whole-cell conductance value $g_{x,max}$ for any type of channel 'x' was divided by the surface area to obtain the maximum conductance density $G_{x,max}$ to allow us to evaluate local current densities at specific sites in the model. The transporters Na^+/K^+-ATPase and KCC were assumed to operate at pseudo-steady state and depend only on $[K^+]$ in the cleft. On the hair cell, basolateral channels were only distributed to the part of the membrane enclosed by the calyx.

Table S6. Currents Densities and Kinetics

MET (Hair Cell Apical)

$$I(X) = g_{bundle,max} \cdot P_{MET} \cdot \left(\phi_H - V_{bundle,rev} - \phi_{endolymph}\right)$$

$$P_{MET} = \left(1 + exp\left(4.05 \cdot \left(0.39 - \frac{X+200}{1000}\right)\right)\right)^{-1} \cdot \left(1 + exp\left(14.5 \cdot \left(0.25 - \frac{X+200}{1000}\right)\right)\right)^{-1}$$

$X = displacement(t)$; Step or sinusoidal functions were used.

Kinetics in the model: (Holt et al. 1997). $V_{bundle,rev}$ is 0 mV (Corns et al. 2014).
$\phi_{endolymph}$ is 5 mV (Köppl et al. 2018; Li et al. 2020).

$g_{K,L}$ (Hair Cell)

$$J_{K,L} = G_{K,L,max} \cdot P_{K,L} \cdot (V_m - E_K)$$

$$G_{K,L,max} = \frac{g_{K,L,max}}{a_{H,C}}$$

$$P_{K,L} = act_{K,L}$$

$$\tau_{K,L} \cdot \frac{d\left(act_{K,L}\right)}{dt} = act_{\infty,K,L} - act_{K,L}$$

$$\tau_{K,L} = 429.7 \cdot exp\left(-0.2826 \cdot \frac{V_m - (-80)}{2.84}\right) + 10$$

$$act_{\infty,K,L} = \left(1 + exp\left(-\frac{V_m - (-80)}{2.84}\right)\right)^{-1}$$

Presence in hair cell: (Rennie and Correia 1994; Rüsch and Eatock 1996).
Activation Kinetics in the model: (Spaiardi et al. 2017, 2020).
$\tau_{K,L}$ is based on measurements of the slow time constant: (Wong et al. 2004; Songer and Eatock 2013; Spaiardi et al. 2017).

g_{Ca} (Hair Cell)

$$J_{Ca} = G_{Ca,max} \cdot P_{Ca} \cdot (V_m - E_{Ca})$$

$$G_{Ca,max} = g_{Ca,max} \,/\, a_{H,C}$$

$$P_{Ca} = act_{Ca}$$

$$\tau_{Ca} \cdot \frac{d(act_{Ca})}{dt} = act_{\infty,Ca} - act_{Ca}$$

$$\tau_{Ca} = 0.6\, ms$$

$$act_{\infty,Ca} = \frac{1}{1 + \exp\left(-\frac{V_m - (-44)}{5.8}\right)}$$

Presence and Kinetics: (Bao et al. 2003), assuming an intracellular $[Ca^{2+}]$ of $1\mu M$.

HCN1 (Hair Cell)

$$J_{K,HCN1} = \frac{4}{5} \cdot G_{HCN1,max} \cdot P_{HCN1} \cdot (V_m - E_K)$$

$$J_{Na,HCN1} = \frac{1}{5} \cdot G_{HCN1,max} \cdot P_{HCN1} \cdot (V_m - E_{Na})$$

$$G_{HCN1,max} = g_{HCN1,max} \,/\, a_{H,C}$$

$$P_{HCN1} = act_{HCN1}$$

$$\tau_{HCN1} \cdot \frac{d(A_{HCN1})}{dt} = act_{\infty,HCN1} - act_{HCN1}$$

$$\tau_{HCN1} = 209.479 + \left(\left(exp\left(-\frac{V_m + 80.646}{6.916}\right)\right)^{-1} + exp\left(\frac{V_m + 80.646}{14.881}\right)\right)/2551.988$$

$$act_{\infty,HCN1} = \frac{1}{1 + exp\left(\frac{V_m - (-90))}{6.8}\right)}$$

Location and Kinetics: (Horwitz et al. 2014), adapted for simple calyx.
τ_{HCN2}: (Ventura and Kalluri 2019), Parameters for the HCN “Max Activation” case.

The K^+ : Na^+ permeability ratio through HCN1 channels is 4:1 (Lee and MacKinnon 2017). The fractions 4/5 and 1/5 in the equations for $J_{K,HCN1}$, and $J_{Na,HCN1}$ reflect this.

Na^+/K^+-ATPase (Hair Cell | Calyx Inner Face | Calyx Outer Face)

$$J_{pump} = (3-2) \cdot \frac{F \cdot 10^{12}}{N_A} \cdot \rho_{NaK} \cdot v_{NaK} \cdot P_{pump}$$

$\rho_{NaK} =$ 1000 | 1000 | 2000 pumps/µm^2

$$P_{pump} = \left(\frac{[K^+]_{SC}}{[K^+]_{SC}+1.5}\right)^2 \Bigg| \left(\frac{[K^+]_{SC}}{[K^+]_{SC}+1.5}\right)^2 \Bigg| \left(\frac{5}{5+1.5}\right)^2 ;$$

Presence of Na^+/K^+-ATPase: (Schuth et al. 2014).
A pseudo-steady state expression was used with v_{NaK} of 100/s, a Hill coefficient of 2 (Jaisser et al. 1994) and a K^+ molar affinity of 1.5 mM, adapted from (Crambert et al. 2000). ρ_{NaK} values were chosen such that the $[Na^+]_{SC}$ at rest, at the base of the cleft, was between 120 – 140 mM with the reasoning that quantal currents occurring at the calyx inner face would require sufficient Na^+ driving forces. In the expression for J_{pump}, 10^{12} is a conversion factor from Coulombs to picoCoulombs.

KCC4 (Calyx Inner Face)

$$J_{KCC4} = J_{KCC4,max} \cdot P_{KCC4}$$

$J_{KCC4,max}$ = 2 pA/µm^2

$$P_{KCC4} = \left(1 + \left(\frac{17.5}{[K^+]_{SC}}\right)^2\right)^{-1}$$

Molar affinity (17.5 mM) from (Mercado et al. 2000). Hill Coefficient based on discussions in (Marcoux et al. 2017). $J_{KCC4,max}$ was chosen such that the $[K^+]_{SC}$ at rest, at the base of the cleft as calculated by the stationary solver was between 5-7 mM. Although J_{KCC4} is expressed as a current, transport activity of KCC is electroneutral and does not contribute to a change in potential. KCC4 was localized to the calyx inner face, see Experimental Methods below.

K_V7.4 (Calyx Inner Face | Calyx Outer Face)

$$J_{K_V7.4} = G_{K_V7.4,max} \cdot P_{K_V7.4} \cdot (V_m - E_K)$$

$$G_{K_V7.4,max} = \frac{\frac{4}{5} g_{K_V7.4,max}}{a_{CIF}} \quad | \quad \frac{\frac{1}{5} g_{K_V7.4,max}}{a_{COF}}$$

$$P_{K_V7.4} = act_{K_V7.4}$$

$$\tau_{K_V7.4} \cdot \frac{d(act_{K_V7.4})}{dt} = act_{\infty,K_V7.4} - act_{K_V7.4}$$

$$\tau_{K_V7.4} = max\left(\left(0.0002488 \cdot exp(-0.04401 \cdot V_m) + 0.4506 \cdot exp(0.05437 \cdot V_m)\right)^{-1}, 1\right)$$

$$act_{\infty,K_V7.4} = \left(1 + exp\left(\frac{V_m - (-52)}{16}\right)\right)^{-1}$$

Location & Kinetics: (Hurley et al. 2006).
In $G_{K_V7.4,max}$, the fractions 4/5 and 1/5 reflect the relative density of the channel on either membrane observed in electron microscope immunogold experiments. See Experimental Methods below.

HCN2 (Calyx Inner Face | Calyx Outer Face)

$$J_{K,HCN2} = \frac{4}{5} \cdot G_{HCN2,max} \cdot P_{HCN2} \cdot (V_m - E_K)$$

$$J_{Na,HCN2} = \frac{1}{5} \cdot G_{HCN2,max} \cdot P_{HCN2} \cdot (V_m - E_{Na})$$

$$G_{HCN2,max} = \frac{\frac{1}{2} g_{HCN2,max}}{a_{CIF}} \mid \frac{\frac{1}{2} g_{HCN2,max}}{a_{COF}}$$

$g_{HCN2,max}$ was distributed equally to both the CIF and COF.

$$P_{HCN2} = act_{HCN2}$$

$$\tau_{HCN2} \frac{d(act_{HCN2})}{dt} = act_{\infty,HCN2} - act_{HCN2}$$

$$\tau_{HCN2} = 209.479 + \left(\left(exp\left(-\frac{V_m + 80.646}{6.916}\right)\right)^{-1} + exp\left(\frac{V_m + 80.646}{14.881}\right)\right)/2551.988$$

$$act_{\infty,HCN2} = \left(1 + exp\left(\frac{V_m + 95}{11.7}\right)\right)^{-1}$$

Presence and Kinetics: (Horwitz et al. 2014). Adapted for a simple calyx.
τ_{HCN2}: (Ventura and Kalluri 2019), Parameters for the HCN "Max Activation" case.
The K^+ : Na^+ Permeability ratio through HCN1 channels is 4:1 (Lee and MacKinnon 2017). The same ratio was assumed for HCN2 channels. The fractions 4/5 and 1/5 in the equations for $J_{K,HCN2}$, and $J_{Na,HCN2}$ reflect this.

I_{Leak} (Calyx Outer Face)

$$J_{Leak} = G_{Leak,max} \cdot (V_m - 0)$$

$$G_{Leak,max} = \frac{g_{Leak,max}}{a_{COF}}$$

$g_{Leak,max}$ was set equal to 2 nS. The value was chosen to compensate for unknown membrane properties and assist in setting the resting calyx potential.

K_V7.x (Hemi-Node | Node)

$$J_{K_V7.x} = G_{K_v7.x,max} \cdot P_{K_V7.x} \cdot (V_m - E_k)$$

$$G_{K_v7.x,max} = \frac{g_{K_V7.x,max}}{a_{F,HN} + 2a_{F,N}}$$

$$P_{K_V7.x} = act_{K_V7.x}$$

$$\tau_{K_V7.x} \cdot \frac{d\left(act_{K_V7.x}\right)}{dt} = act_{\infty,K_V7.x} - act_{K_V7.x}$$

$$\tau_{K_V7.x} = 1.2 \cdot exp(-0.08 \cdot V_m) \cdot \frac{1}{1 + exp\left(-\frac{V_m + 47}{8}\right)}$$

$$act_{\infty,K_V7.x} = \frac{1}{1 + exp\left(-\frac{V_m + 47}{8}\right)}$$

Kinetics: (Kalluri et al. 2010).

K_V3.4 (Hemi-Node | Node)

$$J_{K_V3.4} = G_{K_V3.4,max} \cdot P_{K_V3.4} \cdot (V_m - E_k)$$

$$P_{K_V3.4} = act_{K_V3.4} \cdot inact_{K_V3.4}$$

$$\tau_{K_V3.4,act} \cdot \frac{d\left(act_{K_V3.4}\right)}{dt} = act_{\infty,K_V3.4} - act_{K_V3.4}$$

$$\tau_{K_V3.4,inact} \cdot \frac{d\left(inact_{K_V3.4}\right)}{dt} = inact_{\infty,K_V3.4} - inact_{K_V3.4}$$

$$\tau_{K_V3.4,act} = 5 \cdot 1.41 \cdot exp(-0.05589 \cdot V_m) \cdot \left(1 + exp\left(-\frac{V_m+31.3}{8.5}\right)\right)^{-1}$$

$$\tau_{K_V3.4,inact} = 25.4 \text{ ms}$$

$$act_{\infty,K_V3.4} = \left(1 + exp\left(-\frac{V_m+31.3}{8.5}\right)\right)^{-1}$$

$$inact_{\infty,K_V3.4} = \left(1 + exp\left(\frac{V_m+65.84}{5.51}\right)\right)^{-1}$$

Kinetics: (Chabbert et al. 2001). $G_{K_V3.4,max}$ was adapted to a value of 0.2 nS/µm^2 and is comparable to the values for $G_{K_V1.x,max}$ and $G_{K_V7.x,max}$.

K_v1.x (Hemi-Node | Node)

$$J_{K_V1} = G_{K_V1,max} \cdot P_{K_V1} \cdot (V_m - E_k)$$

$$G_{K_v1.x,max} = \frac{g_{K_V1.x,max}}{a_{F,HN} + 2a_{F,N}}$$

$$P_{K_V1} = act_{K_V1}$$

$$\tau_{K_V1} \cdot \frac{d\left(act_{K_V1}\right)}{dt} = act_{\infty,K_V1} - act_{K_V1}$$

$$act_{\infty,K_V1} = \frac{1}{1 + exp\left(-\frac{V_m + 44}{7.1}\right)}$$

$$\tau_{K_V1} = 3.7\ ms$$

Kinetics: (Kalluri et al. 2010).

Na_v (Unmyelinated|Hemi-Node | Node)

$$J_{Na_V} = G_{Na_V,max} \cdot P_{Na_v} \cdot (V_m - E_{Na})$$

$$J_{Na_V,Unmyel} = \frac{1}{4} \cdot G_{Na_V,max} \cdot P_{Na_v} \cdot (V_m - E_{Na})$$

$$G_{Na_V,max} = g_{Na_V,unitary} \cdot \rho_{Na_V}$$

$$P_{Na_V} = act_{Na_V} \cdot inact_{Na_V}$$

$$\tau_{Na_V,act} \cdot \frac{d\left(act_{Na_V}\right)}{dt} = act_{\infty,Na_V} - act_{Na_V}$$

$$\tau_{Na_V,inact} \cdot \frac{d\left(inact_{Na_V}\right)}{dt} = inact_{\infty,Na_V} - inact_{Na_V}$$

$$\tau_{Na_V,act} = \left(1 + \exp\left(-\frac{V_m + 41.58}{5.733}\right)\right)^{-1} \left(1 + \exp\left(\frac{V_m + 8.295}{16.28}\right)\right)^{-1} + 0.2$$

(for -55 $\leq V_m \leq 60\ mV$); 0.2 ms otherwise.

$$\tau_{Na_V,inact} = 0.0001452\ exp(-0.2211\ V_m) + 0.2382$$

(for -45 $\leq V_m \leq 60\ mV$); else, linearly extrapolated.

$$act_{\infty,Na_V} = \left(1 + exp\left(-\frac{V_m+40}{8}\right)\right)^{-1}$$

$$inact_{\infty,Na_V} = \left(1 + exp\left(\frac{V_m+69}{7.6}\right)\right)^{-1}$$

Kinetics: (Liu et al. 2016; Meredith and Rennie 2018).
$\tau_{Na_V,act}$ and $\tau_{Na_V,inact}$, see Experimental Methods below.
A reduced channel density was assumed at the unmyelinated segment and the maximum conductance density reduced to ¼ of the full value. This reflects evidence for greater channel clustering near regions adjacent to myelinated segments of fiber (Freeman et al. 2016).

Table S7 - Sources

Model Compartment	Property	Reference	Animal	Location	Age
General	Calyx Dimensions	(Lysakowski et al. 2011) Fig. 2C – central calyx-only afferent	Rat	SCC	6 Months
Hair Cell	MET	(Holt et al. 1997)	Mouse	Utricle	P1 - P10
	MET, P_0 = 10%	(Songer and Eatock 2013)	Rat	Saccule	P1 - P9
	MET, 5nS	(Holt et al. 1997)	Mouse	Utricle	P1 - P10
	$g_{K,L}$	(Spaiardi et al. 2017)	Mouse	SCC	P6 - P19
	$\tau_{g_{K,L}}$ Fit of slow time constant	(Wong et al. 2004)	Rat	Utricle	P16 - P24
		(Songer and Eatock 2013)	Rat	Saccule	P1 – P9
		(Spaiardi et al. 2017)	Mouse	SCC	P6 - P19
	gCa	(Bao et al. 2003)	Rat	SCC	P4 - P20
	HCN1	(Horwitz et al. 2011)	Mouse	Utricle	P0 - P25
HC/Calyx	Na^+/K^+-ATPase	(Schuth et al. 2014)	Rat	Utricle/SCC	P17– P25
	τ_{HCN}	(Ventura and Kalluri 2019) - HCN Max Activation parameters	Rat	VGN	P9 - P21
Calyx	HCN2	(Horwitz et al. 2014)	Mouse	Utricle	P0 - P25
	$K_v7.4$	(Hurley et al. 2006)	Rat	Utricle	P2 - P26
		(Lysakowski et al. 2011)	Rat	Utricle/SCC	6 Months
	KCC4	See Experimental Methods	Rat	SCC	6 months
		(Mercado et al. 2000)	Frog Oocyte	(expressing mouse KCC4)	Day 5
		(Marcoux et al. 2017)	Various mammals	-	-
Fiber	HN, N1 Location	(Lysakowski et al. 2011)	Rat	Utricle, Saccule and SCC	6 Months
	Na_V	(Liu et al. 2016)	Rat	VGN	P1 - P8
		(Meredith and Rennie 2018)	Gerbil	SCC	P5 - P31
	K_v7	(Kalluri et al. 2010)	Rat	VGN	P8 - P15
	K_v1	(Kalluri et al. 2010)	Rat	VGN	P8 - P15
	$K_v3.4$	(Chabbert et al. 2001)	Mouse	VGN	P5 - P8

SCC – Semicircular Canal Crista. Utricle and saccule reference their maculae. Conductance values are presented in **Table S5** and kinetics are presented in **Table S6**.

EXPERIMENTAL METHODS

Below we describe the experimental methods used to determine unpublished parameters listed in the Tables, and imaged cells shown in **Fig. 1A**.

Na_V time constants (Table S6): Whole-cell patch clamp recordings from mouse vestibular afferent neurons. The kinetics of postsynaptic (afferent) Na_V currents were obtained from mouse vestibular ganglion neurons isolated in the first postnatal month. Animals were handled in accordance with the *National Institutes of Health Guide for the Care and Use of Laboratory Animals*, and all procedures were approved by the animal care committee at the University of Chicago. Mice were deeply anesthetized with isoflurane and decapitated. Vestibular ganglia were dissected out and mechanically dissociated following enzymatic digestion (with 0.12 % collagenase and 0.12% trypsin for 15-20 minutes at 37°C) and cultured overnight to remove satellite cells, in minimal essential medium with Glutamax (MEM, Invitrogen, Carlsbad, CA) supplemented with 10 mM HEPES, 5% fetal bovine serum (FBS), and 1% penicillin in 5% CO_2-95% air at 37°C.

Whole-cell patch clamp recordings were made with solutions designed to minimize contamination from K^+ and Ca^{2+} currents. The external medium comprised (mM): 75 NaCl, 5.4 CsCl, 2.5 $MgCl_2$, 75 TEACl, 5 HEPES, 10 D-glucose, titrated with CsOH to pH 7.4, with osmolality ~310 mmol/kg. The internal (pipette) solution contained: 148 CsCl, 0.8 CaCl, 3.5 Na_2-creatine phosphate, 3.5 MgATP, 0.1 LiGTP, 5 EGTA, 5 HEPES, 0.1 Na-cAMP, titrated with CsOH to pH 7.4, and ~300 mmol/kg. Recordings were made at room temperature (23-25℃). Signals were delivered and recorded with a Multiclamp 700B amplifier, Digidata 1440A digitizer, and pClamp 10 or 11 software (Axon Instruments, Molecular Devices, Sunnyvale, CA), with low-pass Bessel filtering set at 10 kHz and sampling interval set at 5 µs. Seal resistance exceeded 1 GΩ.

Membrane voltages were corrected off-line for a measured liquid junction potential of 6.4 mV and for series resistance errors. Analysis was performed with MATLAB (The MathWorks, Natick, MA), Clampfit (Axon Instruments, Molecular Devices) and Origin Pro 2018 (OriginLab, Northampton, MA). Series resistance (R_S) ranged between 3 and 10 MΩ and was compensated by 75%. The holding potential was −66.4 mV. Activation and inactivation time courses were measured for currents evoked by depolarizing voltage steps following a pre-pulse to −127 mV to de-inactivate Na_V current. The currents were fit with the following Hodgkin-Huxley equations for Na_V channel activation (n=6) and inactivation (n=9): $I(t) = I_{peak}\left(1 - e^{-\frac{t}{\tau_m}}\right)^3$; $I(t) = I_{SS} + I_{peak}(e^{-t/\tau_h})$ where I is current, t is time; I_{peak} and I_f are peak and steady-state (inactivated) currents, respectively; and τ_m and τ_h are the time constants for the activation and inactivation transitions, respectively.

Location of KCC, relative density of K_V7.4 (Table S6) and image of hair cells and calyces (Fig. 1A): Confocal microscopy and immunocytochemistry

Fixation. Animals were handled in accordance with the *National Institutes of Health Guide for the Care and Use of Laboratory Animals*, and all procedures were approved by the IACUC at the Univ. of Illinois at Chicago. Long-Evans rats (Charles River Laboratories, Wilmington, MA) were deeply anesthetized with Nembutal (80 mg/kg), then perfused transcardially for 1 min with physiological saline containing heparin (2000 IU), followed by a dialdehyde fixative for 10 min (4% paraformaldehyde, 1% acrolein, 1% picric acid, and 5% sucrose in 0.1 M phosphate buffer (PB), pH 7.4). After decapitation, the head was post-fixed in the fixative for 20 min and then placed in 30% sucrose in 0.1 M PB. Vestibular and auditory organs were dissected out with the head immersed in PB. Decalcification of cochleas and removal of bone debris and otoliths from vestibular organs was accomplished through incubation in Cal-X solution. Background fluorescence was reduced by incubating the tissues in a 1% aqueous solution of sodium borohydride for 10 min. All organs were then placed in 30% sucrose in 0.1 M PB overnight.

Immunohistochemistry. Dissected tissues were gelatin-embedded and cut with a freezing sliding microtome. Tissue permeabilization was carried out with 4% Triton X-100 in PBS for 1 hr, and a blocking solution composed of 0.5% fish gelatin, 0.5% Triton X-100 and 1% BSA in 10 mM phosphate-buffered saline (PBS) was used for 1 hr. Samples were incubated in primary antibodies diluted 1:200 in blocking solution: goat anti-calretinin (AB1550), rabbit anti-KCC4 (AB3270) (all available or formerly available from Chemicon/Millipore-Sigma, St. Louis, MO) or rabbit anti-myosin 6 (a generous gift from Dr. Tama Hasson). The anti-calretinin antibody served as a marker of type II hair cells and calyx afferents (Desai et al. 2005a, 2005b). Specific labeling was revealed with these secondary antibodies (1:200 in the blocking solution): FITC-conjugated donkey anti-goat and rhodamine-conjugated donkey anti-rabbit (both from Chemicon, Temecula, CA). Sections were mounted on slides using a medium containing Mowiol (Calbiochem, Darmstadt, Germany) and examined on a confocal microscope (LSM 510 META, Carl Zeiss, Oberköchen, Germany). The relative density of Kv7.4 channels was based on electron microscopic (EM) immunogold experiments, with methods described in Hurley et al. (2006). In brief, 40-μm vibratome sections were incubated in primary antibody [1:200 rabbit anti-KCNQ4, a generous gift from Dr. Bechara Kachar] for 72 h and secondary antibody (1:50; colloidal gold-labeled goat anti-rabbit IgG; Amersham Biosciences, Piscataway, NJ) for 24 h. Colloidal gold staining was silver enhanced (4–8 min; IntenSE M kit; Amersham Biosciences). For more details, see Hurley et al. (2006).